

MXene Printing and Patterned Coating for Device Applications

Yi-Zhou Zhang, Yang Wang, Qiu Jiang, Jehad K. El-Demellawi, Hyunho Kim, and Husam N. Alshareef*

As a thriving member of the 2D nanomaterials family, MXenes, i.e., transition metal carbides, nitrides, and carbonitrides, exhibit outstanding electrochemical, electronic, optical, and mechanical properties. They have been exploited in many applications including energy storage, electronics, optoelectronics, biomedicine, sensors, and catalysis. Compared to other 2D materials, MXenes possess a unique set of properties such as high metallic conductivity, excellent dispersion quality, negative surface charge, and hydrophilicity, making them particularly suitable as inks for printing applications. Printing and pre/post-patterned coating methods represent a whole range of simple, economically efficient, versatile, and eco-friendly manufacturing techniques for devices based on MXenes. Moreover, printing can allow for complex 3D architectures and multifunctionality that are highly required in various applications. By means of printing and patterned coating, the performance and application range of MXenes can be dramatically increased through careful patterning in three dimensions; thus, printing/coating is not only a device fabrication tool but also an enabling tool for new applications as well as for industrialization.

devices. This is because solution processes such as liquid-phase exfoliation is crucial for the dispersion formation and mass production, as well as for the postsynthesis treatments on the 2D nanosheets such as sorting in terms of flake size and thickness, functionalization, compositing, etc., all of which are crucial for the ink formulation process required by printing.^[6] Printed electronics technology has acquired considerable interest from both academia and industry recently.^[7–9] Unlike traditional methods such as vacuum deposition and photolithography, printing technologies hold great promise for fast, high-volume, and low-cost manufacturing, especially for the fabrication of flexible devices.^[10–15] The combination of 2D materials with printing started as early as 2012 when liquid-phase-exfoliated graphene dispersion was inkjet-printed to fabricate field-effect transistors.^[16] It has since progressed from directly using the unopti-

1. Introduction


2D nanomaterials have drawn significant attention among the materials research community in the past decade because of their fascinating and often unique physical and chemical properties, as well as their high application potential to tackle society's most pressing issues.^[1–3] The recent fast development of solution-processed 2D nanomaterials has sparked a great interest toward the field of printed electronics,^[4,5] which means applying printing technologies from the graphic industry (e.g., screen, gravure, inkjet printing) to the fabrication of electronic

mized dispersion obtained from the solution processing as inks to making formulated inks targeted toward specific printing methods and target applications (e.g., conductive tracks, transparent electrodes, transistors, photodetectors, energy storage devices such as supercapacitors, batteries, sensors, etc.).^[17–21]

As a new member to the 2D nanomaterials family, transition metal carbides, nitrides, and carbonitrides, also known as MXenes, possess outstanding electrochemical, electronic, optical, and mechanical properties, and thus have shown great promise in applications including energy storage, electronics, optoelectronics, biomedicine, sensors, and catalysis.^[22–25] Research on MXenes dates back to 2011 when single-layered titanium carbide Ti_3C_2 was synthesized and separated for the first time,^[26] and has since evolved into a worldwide joint effort dealing with a material family of almost 30 members. The general formula of MXenes is $\text{M}_{n+1}\text{X}_n\text{T}_z$ ($n = 1, 2, \text{ or } 3$) or $\text{M}_{1.33}\text{XT}_z$, where M is an early transition metal, X represents carbon, and/or nitrogen, and T refers to the various terminations such as fluorine, hydroxyl, and/or oxygen atoms. The free electrons of the transition metal carbide/nitride backbone endow MXenes with metallic conductivity; on the other hand, the abundant surface functional groups make MXenes hydrophilic. Unlike other 2D materials which mainly rely on mechanical exfoliation or bottom-up methods such as chemical vapor deposition (CVD) to obtain high-quality nanosheets; MXenes are mostly synthesized

Dr. Y.-Z. Zhang, Dr. Q. Jiang, J. K. El-Demellawi, H. Kim, Prof. H. N. Alshareef
Physical Sciences and Engineering Division
Materials Science & Engineering
King Abdullah University of Science and Technology (KAUST)
Thuwal 23955-6900, Kingdom of Saudi Arabia
E-mail: husam.alshareef@kaust.edu.sa

Y. Wang
University of Twente
MESA+ Institute for Nanotechnology
P. O. Box 217, Enschede 7500 AE, The Netherlands

 The ORCID identification number(s) for the author(s) of this article can be found under <https://doi.org/10.1002/adma.201908486>.

DOI: 10.1002/adma.201908486

by selective etching of the A element (group IIIA to VIA) from the MAX phases, followed by exfoliation into nanosheets, both two steps are conducted in dispersions.^[27] This subtle difference between MXenes and other 2D materials has one significant implication, i.e., MXenes are inherently compatible with solution-based deposition/patterning methods, which brings printing of MXenes to the spotlight. Although printing methods such as inkjet, screen, and 3D printing are the most straightforward answers that come into mind when one thinks about deposition/patterning of MXenes from dispersions, the high requirements in terms of facility, expertise, and ink rheology present tremendous difficulty for researchers. Instead, we have noticed some smart, yet simple modified coating methods coming up in the literature that show great promise for patterning MXenes including spray coating assisted with shadow masks or laser cutting, masked vacuum filtration, writing MXenes inks using daily writing tools, etc. Thus, although this review focuses on printing MXenes, some pre/post-patterned coating methods are also included.

MXenes possess some exciting and unique properties that make them particularly suitable as inks for printing and patterned coating. First, MXene flakes possess hydrophilicity due to the surface functional groups such as $-O$, $-F$, and $-OH$; on the other hand, MXene flakes are highly negatively charged (zeta potential of about -30 mV), and can easily form stable colloidal dispersions in various aqueous and organic solvents.^[25] These two properties make aqueous dispersion of MXenes easy to obtain. This is particularly important in the context of environmental-friendly printing, where no organic solvents should be involved. Interestingly, $Ti_3C_2T_x$, as a typical example of MXenes, is surprisingly stable in aqueous dispersions with a large concentration window from less than 1 to hundreds of $mg\ mL^{-1}$, without the use of any surfactant which is often required for the formulation of printable inks.^[27,28] This is significant for printing because the residual surfactants may compromise the electronic properties of the printed/coated films and thus need to be removed by postprinting treatments, usually by heat, which limits the available flexible substrates for printing. On the other hand, the large concentration window where MXenes remain stable precludes the use of rheology modifiers, which are commonly used for the printing of functional materials, making tuning of MXene inks in terms of rheology and concentration much easier. Their characteristic stable dispersion also facilitates tuning the morphological properties (flake size, defects, etc.) of MXenes by sonication or intercalation with ions/molecules, which has significant influence on the physical properties of MXenes.

Thus, for MXenes, printing and patterned coating mean more than just a set of versatile, scalable, reproducible, and cost-effective patterning methods, but rather a key factor that researchers working on MXenes need to pay attention to throughout the synthesis, modification, and application process cycle. For instance, achieving complex 3D architectures and multifunctionality that are highly required in some applications requires a detailed design for each preparation step, starting from the etching and delamination stages. In this sense, by using printing or patterning-assisted coating, the performance and application range of MXenes can be dramatically increased through careful patterning in three dimensions; thus, printing/



Yi-Zhou Zhang received his bachelor's degree from Nanjing University, after which he obtained a Ph.D. from Nanjing University of Posts and Telecommunications under the supervision of Prof. Wei Huang. He is currently a postdoctoral fellow in Prof. Husam N. Alshareef's group at KAUST. He has been

focusing on printed energy storage and electronics since the beginning of his research career; after he joined Prof. Alshareef's group, he has been exploring MXenes for new applications.



Husam N. Alshareef is a professor of materials science and engineering at KAUST. After nearly ten years in the semiconductor industry, he joined KAUST in 2009 where he initiated an active research group working on semiconductor nanomaterial development for energy storage and electronics.

coating is not only a device fabrication/patterning tool but also an enabling tool for new applications as well as for industrialization. As a result, we have seen exponential growth in high-quality publications regarding printing and patterned coating of MXenes in the past two years, turning this into a highly competitive field of research, yet there is no literature summarizing this exciting fast-moving field. Here we provide this timely summary not only to show the great utility of printing/coating methods in improving the performance of MXene-based devices but also to suggest the great potential of those methods in realizing new possibilities for MXenes. This review appeals not only to researchers searching for large-scale, versatile, environmental-friendly, and low-cost manufacturing technology for devices based on MXenes, but also to those studying 2D nanomaterials for various applications such as optoelectronics, catalysis, microelectronics, sensing, etc., and those interested in printed electronics and flexible electronics in general. With this in mind, we construct this review as follows (**Figure 1**): we first discuss how to turn MXenes into inks, mainly focusing on the issues that are important for printing, including etching of MAX and delamination of etched MAX into MXenes, the rheology of MXene inks and how to tune the rheological and morphological properties of MXenes, and how to increase the stability of MXenes inks as well as properly storing them for long time. We then introduce a variety of printing/coating techniques that are relevant for MXenes, mainly inkjet, screen, transfer, direct ink writing (DIW), 3D printing, and patterned

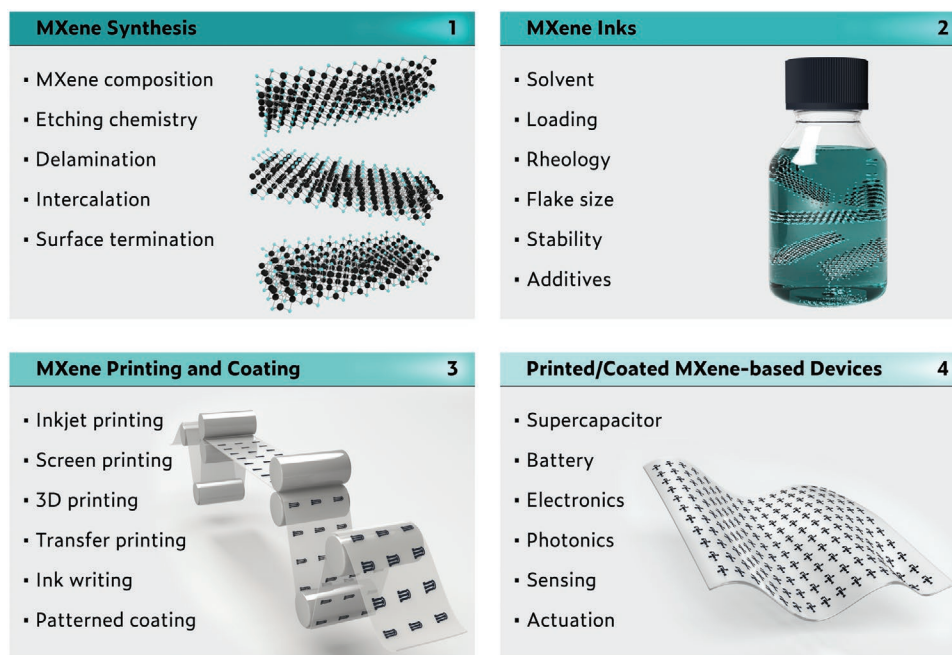


Figure 1. Schematics showing the critical elements for the realization of printed/coated MXene devices. The synthesis of MXene, optimization of ink formulations, printing/coating processes, and device fabrications all have to be collectively optimized.

coating methods. In the fourth section, we discuss recent work on printing and patterned coating of MXenes in terms of applications (energy storage, electronics and optoelectronics, sensing and actuation). Lastly, we present our views on the current status and future directions in this interesting field.

2. Turning MXenes into Inks

2.1. Etching of MAX

MXenes are produced by selectively removing the “A” layers from their parent laminated MAX phases; MAX phases are ternary carbides and nitrides that have a general formula of $M_{n+1}AX_n$. This etching process is possible because the metallic M–A bond is much more chemically active than the M–X bond.^[22] In the first successful production of MXene,^[26] Ti_3AlC_2 powders were immersed in hydrofluoric acid (HF), and the Al layer was extracted from the MAX phases (Figure 2a,b), by breaking the hydrogen bonds between the MXene flakes, the as-obtained multilayer MXene powders can be further converted to stacked MXenes after sonication in methanol. Since then, the wet-chemical etching method has been widely used to produce MXenes. The same HF etching method has been used to exfoliate Ti_2AlC , Ta_4AlC_3 , $(Ti_{0.5}Nb_{0.5})_2AlC$, $(V_{0.5}Cr_{0.5})_3AlC_2$, Ti_3AlCN ,^[29] and Nb_4AlC_3 .^[30] The optimal etching conditions for different MAX phases depend on the atomic bonding strength, particle size, and crystal structures. Generally, larger atomic number transition metal (M) requires longer etching time and stronger etchant.^[25] The intercalation and delamination of MXene was first reported in 2013 when single-flake $Ti_3C_2T_x$ MXene sheets were separated by dimethyl sulfoxide

intercalation followed by sonication (Figure 2c).^[31] This resulted in well-dispersed MXene suspension, which enables the fabrication of free-standing MXene “paper” and MXene inks that can be printed/coated. To date, various etching and delamination methods have been reported to produce more than 20 different MXenes, and dozens are predicted to exist.^[24]

2.2. Delamination of “Etched MAX” into MXene

To decrease the usage of the hazardous HF solution, researchers have tried the acid mixture of HF and HCl with lower HF concentration for etching MAX phases. For example, by etching with low concentration (5 wt%) HF for 24 h can produce MXene with similar quality as compared to the products obtained using 10 wt% HF for 18 h and 30 wt% HF for 18 h.^[27] Bifluoride (NH_4HF_2) salt is another etchant for Ti_3AlC_2 ,^[34] however, the intercalation of NH_4^+ also introduces more H_2O molecules into the MXene layers, which makes the drying of the product more difficult. Alternatively, in situ HF formation from fluoride-containing salts and strong acids can also be used to synthesize MXenes. A mixture of lithium fluoride and hydrochloric acid has proven to be an effective etchant for Ti_3AlC_2 .^[35] Due to the presence of Li^+ , intercalation of cations happens during the etching process, which leads to the formation of MXene “clay.” The ratio of LiF to MAX plays a critical role in the quality of the final product. Lipatov et al. showed that larger MXene flakes with fewer defects could be obtained by changing the ratio of LiF to MAX from 5:1 to 75:1, which results in a lower resistivity and better field-effect electron mobility.^[36] Since no sonication is required in the LiF-HCl etching process, it is also known as the “minimally intensive

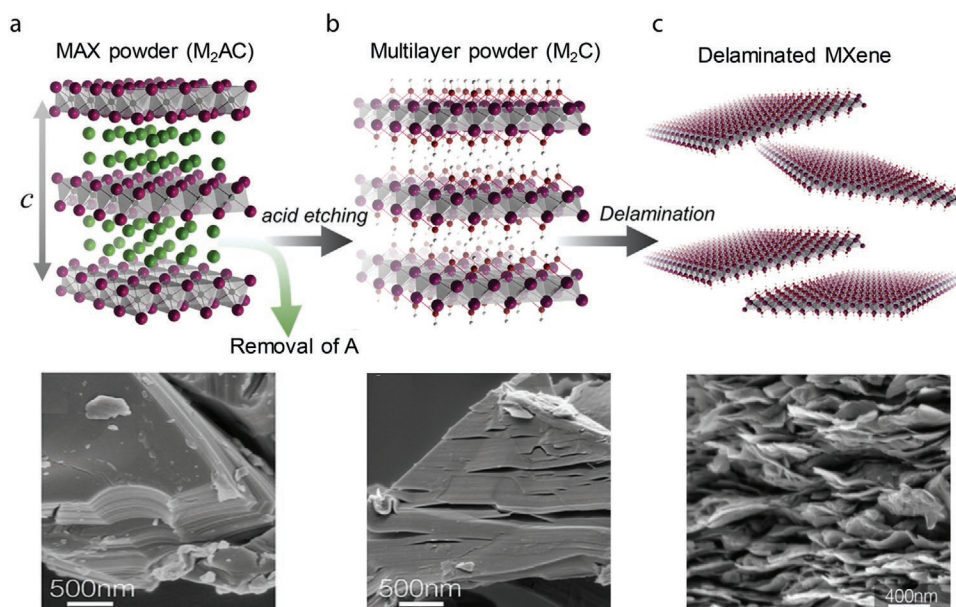
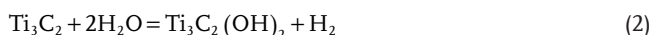
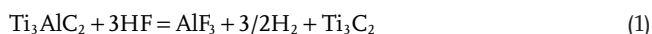


Figure 2. Pathways to synthesize MXene flakes using a top-down etching method. Generally, “A” atomic layer in a) layered MAX phase powders can be selectively removed by hydrofluoric acid (HF), bifluoride-based etchants (NH_4HF_2) or HF-containing salt; this produces b) multilayered MXene powders. Further intercalation of metal cations, DMSO, and TBAOH, followed by sonication, result in c) delaminated single-flake MXene suspensions. Top row) Reproduced with permission.^[32] Copyright 2016, Wiley-VCH. Bottom row) Reproduced with permission.^[33] Copyright 2015, American Chemical Society.

layer delamination (MILD)” method. Molten salt is another type of fluoride-free etchant for the synthesis of MXenes. The use of molten salt as etchant dates back to 1999, when molten cryolite was used to etch the Si atoms from the basal planes of Ti_3SiC_2 .^[37] Urbankowski et al. first showed the successful etching of Al from Ti_4AlN_3 powders by heating it with fluoride salt (a mixture of potassium fluoride (KF), lithium fluoride (LiF), and sodium fluoride (NaF)), the product can be further delaminated to produce Ti_4N_3 MXene. There are also approaches that completely avoid the use of fluorine, e.g., an alkali treatment method was developed, where a hydrothermal treatment of Ti_3AlC_2 in concentrated sodium hydroxide resulted in Ti_3C_2 with high purity.^[38]

2.3. Formulation of MXene Inks

The surface chemistry of materials greatly influences the attractive forces within dispersion and between liquid and the substrate. Thus it is critically important to understand MXene surface chemistry for the stability of the ink and printing process. Based on first-principle calculations, all MXenes with surface terminations are predicted to have negative formation energy with significant thermodynamic stability as compared with bare MXene surfaces.^[39] Thus, MXenes that are synthesized from wet chemistry methods are typically terminated with $-\text{OH}$, $-\text{O}$, and $-\text{F}$ functional groups, which were proposed to originate from the following etching processes^[26]



While the $-\text{O}$ terminations are proposed to originate from the decomposition of $-\text{OH}$ into H_2O and $-\text{O}$. The introduction of surface terminations is predicted to transform MXenes (Sc_2CF_2 , $\text{Sc}_2\text{C}(\text{OH})_2$, Sc_2CO_2 , Ti_2CO_2 , Zr_2CO_2 , and Hf_2CO_2) from metallic to narrow-bandgap semiconductors.^[40] To further improve the electronic properties of MXenes, vacuum annealing process was reported to be an effective method to partially remove the surface terminations and improve the electronic conductivity of the MXenes.^[41] The concentration of the surface terminations is largely dependent on the etching conditions, while the delamination process and postsynthesis treatment also play a vital role in the oxidation of the MXene flakes. Generally, when etched with a higher concentration of HF, more fluorine and less oxygen functional groups were observed.^[25] These functional groups lead to negative zeta potentials and a hydrophilic surface of MXenes. These characteristics lead to a stable suspension of MXene flakes without adding any surfactant and rheology modifier, which is crucial for the direct printing of MXene inks.

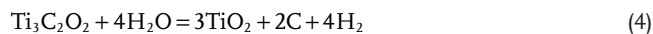
The properties of the synthesized MXenes are highly dependent on the size of the 2D sheets, and some printing methods have strict requirements on the maximum lateral size of the MXene nanosheets. For example, Kayali et al. have demonstrated improved electrochemical performance by controlling the size distribution of MXene flakes.^[42] MXene flakes produced after delamination have a diverse lateral size distribution ranging from nanometers to micrometers. To obtain uniform size distribution, centrifugation is commonly used.^[43] For example, Maleski et al. investigated the correlation between flake size and properties of MXene flakes by developing a density gradient centrifugation to precisely sort MXenes into different flake sizes.^[44] After centrifuging MXene suspension with a layered sucrose density gradient, small flakes were located on the top part of the dispersion,

and large flakes settled to the bottom. It was found that smaller flakes exhibited lower conductivity as compared to larger flakes, which can be attributed to the contact resistance between the flakes and the defects on the edges. Similarly, MXenes with different flake sizes also showed different optical properties, i.e., the UV–visible absorption spectra showed that smaller flakes exhibit decreased absorption in the visible wavelength range. Unlike electrical and optical properties that showed linear correlations with flake sizes, MXene film with a flake size of $\approx 1\ \mu\text{m}$ showed the best electrochemical performance among different films ranging from 0.13 to $4.4\ \mu\text{m}$. At a scan rate of $2\ \text{mV s}^{-1}$, it showed capacitance of $293\ \text{F g}^{-1}$ with good capacitance retention. These results show that there is a trade-off between electrical conductivity and accessible active sites for different flake sizes.

2.4. Chemical Stability and Storage of MXenes Inks

MXene suspensions are known to exhibit very good dispersion quality in many solvents, especially in water.^[27,45–47] However, previous reports have shown that the oxygen dissolved in water plays a vital role in the chemical degradation process of delaminated MXene flakes dispersed in aqueous solutions.^[47,48] Typically, this degradation process is further aggravated for colloidal suspensions of single/few-layered MXenes, owing to their higher surface-area-to-volume ratio, making them highly prone to oxidation. This, in turn, would lead to the structural breakdown and the reduction of the shelf life of the formulated MXene inks as a result of the unconstrained formation of transition metal oxides on the surface of MXenes, e.g., TiO_2 on the surface of $\text{Ti}_3\text{C}_2\text{T}_x$. Such phase transformation and structural deformation get even worse at elevated temperatures or when the MXene dispersions are exposed to light.^[27,46]

In principle, the oxidation begins on the edges of the MXene flakes and grows toward the whole basal plane, thus smaller flakes with more active sites are more prone to oxidation. Oxidation occurs in all forms of media including air, liquid, and solid media, with the fastest rate being in liquid media while the slowest is in solid media.^[49] Thus, eliminating the dissolved oxygen in water by saturating it with nitrogen or argon is an effective way to suppress oxidation. Nonetheless, apart from the dissolved oxygen, water itself remains to be another mild oxidant of MXenes. In this regard, the degradation rate caused by the H_2O -induced oxidation was found to be significantly slowed down by refrigeration.^[27] For instance, it was found that MXene suspensions stored under Ar, at low temperature, only degraded by 1.2% after 25 days, where the possible oxidation was explained as^[47]



Accordingly, for prolonged storage of stable MXene inks, it is now common to store them inside Ar-sealed vials, away from light and below the refrigeration temperature ($<4\ ^\circ\text{C}$).^[46]

However, regardless of the aforementioned exerted efforts to hinder the degradation rate of MXenes in water, still, they are not perfectly sufficient for long-term storage. Hence, storing MXenes in organic solvents seems to be a better choice owing to the stabilization solvation effect offered by organic solvents.^[27,45] It was shown that well-suspended MXene dispersions in organic solvents remained stable for several months.^[45]

Another practice was suggested to completely prevent the oxidation of MXenes by filtrating the suspensions and storing the obtained dried films under vacuum. In such a case, MXene inks can be obtained when needed by redispersing the stored MXene films in the desired solvent.^[27,47] However, it is worth mentioning that the drying process can cause the restacking of the delaminated nanosheets, similar to other 2D materials, especially if dried at high temperatures. Thus, to extend the shelf life of MXene suspensions, while avoiding the restacking issue, Zhao et al. found that antioxidants such as sodium L-ascorbate can prevent the oxidation of $\text{Ti}_3\text{C}_2\text{T}_x$ even in the presence of oxygen and water.^[50] Sodium L-ascorbate was found to be associated with the positively charged edges of the MXene flakes, restricting reactions between edge sites and water molecules. Following the treatment with antioxidants, the chemical stability, colloidal stability, chemical compositions, and conductivity were all well preserved after 21 days of continuous exposure to water and oxygen. The active edge sites of MXene flakes can also be capped by polyanionic salts such as polyphosphates, polyborates, and polysilicates,^[51] which can suppress the oxidation of MXene flakes for more than three weeks in water. The ease of washing and low cost of these polyanionic salts also make the large-scale production and long-term storage of MXene inks possible.

2.5. Rheological Properties of MXene Inks

The physical behavior of MXenes under applied stresses defines the rheological properties of MXene inks, which significantly affect the available printing techniques and the reproducibility of the printing process as well as the quality of printed patterns.^[52] The flow behavior of a liquid is described by the relationship of its viscosity (η) versus shear rate (Figure 3a). Generally, both pseudoplastic and thixotropic properties describe shear-thinning liquids, which are desirable for various printing/coating techniques such as screen printing, spray coating, and extrusion-printing. A liquid with these two behaviors can flow through the printer nozzle when a force is applied and recover its high viscosity immediately after leaving the nozzle when force is released, resulting in the maintenance of the desirable patterns after printing. However, it is worth noting that the rheological requirements for different printing/coating methods vary greatly, e.g., from viscous paste for extrusion 3D printing and screen printing to low-concentration dispersion for inkjet printing. The rheological properties of MXenes can be studied by conducting shear experiments for both single-layer MXene flake suspension and multi-layer MXene dispersions with different concentrations (Figure 3b,c).^[52] Both suspensions showed apparent shear-thinning behaviors, while increased viscosity was observed when concentrations increased. The ratio of elastic modulus to viscous modulus (G'/G'') is another important parameter to determine the rheology of dispersion. For example, spray coating often requires high processing rates with high viscous modules, while extrusion printing needs high elastic modules to preserve the shape of the patterns. As shown in Figure 3d,e, single- and multi-layer MXenes show distinct rheological behaviors, and the wide range of rheological properties of dispersions with different concentrations provide different printing possibilities for the MXene inks. Other than

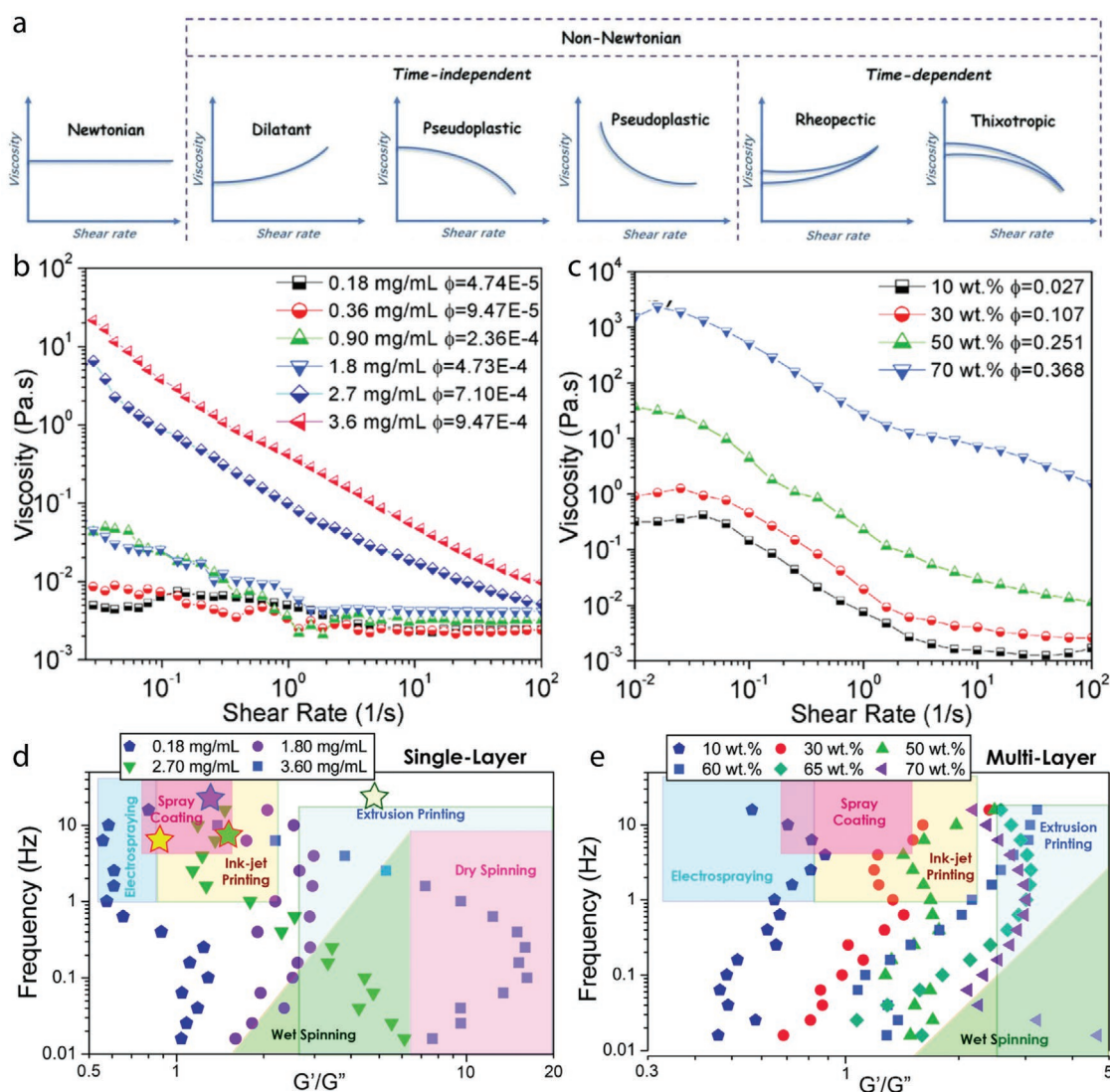


Figure 3. b,c) Measured viscosity versus the shear rate of single-layer MXene flake suspension (b) and multi-layer MXene dispersion (c). d,e) Frequency dependence of the ratio of the G' elastic modulus to G'' viscous modulus for single-layer $\text{Ti}_3\text{C}_2\text{Tx}$ MXene flakes (d) and multilayer $\text{Ti}_3\text{C}_2\text{Tx}$ MXene particles (e) dispersed in water, different features for different printing methods in the literature are summarized in the shaded areas. b–e) Reproduced with permission.^[52] Copyright 2018, American Chemical Society.

low-concentration single-layer MXene dispersions (<10 mg), the rheological properties of concentrated single-layer MXene dispersions have also been studied.^[28,53,54] Interestingly, Yang et al. found that the viscosity values of single-layer MXene dispersions (15 mg mL^{-1}) were on the similar order of magnitude as highly concentrated multilayer MXene dispersions (2.33 g mL^{-1} , 70 wt%),^[54] which means MXene flakes with higher aspect-ratio can tune the rheology more effectively. Using the vacuum evaporation method, they have prepared MXene dispersion with a high concentration of up to 50 mg mL^{-1} . When the shear stress is below a critical point (yield stress), G' is higher than G'' , indicating a typical elastic solid. As the shear stress is increasing above yield stress, G'' starts to be higher than G' , and the ink transits from solid-like behavior to liquid-like behavior. Their ink shows elastic modulus and yield stress of 36 507 and 206 Pa, respectively. Further, Fan et al. prepared nitrogen-doped

Ti_3C_2 dispersion with concentration up to 300 mg mL^{-1} , while the shear stress was found to be reduced to 170 Pa.^[53] Unlike these two reports, Orangi et al. demonstrated high-concentration single-layer MXene dispersion (290 mg mL^{-1}) by using superabsorbent polymer beads,^[28] and they reported yield stress of 24 Pa, which was derived from the Herschel–Bulkley model. While at rest, the ink shows apparent viscoelastic behavior, because G' was always higher than G'' within the entire range of frequency (low-frequency region probes the long-time microstructural rearrangement, and high-frequency region probes shorter time scales), in agreement with other reports.

To enable matching of the surface tension between inks and substrates, MXenes should ideally be dispersed in different solvents. It has been shown that $\text{Ti}_3\text{C}_2\text{Tx}$ can be dispersed in various polar organic solvents such as *N,N*-dimethylformamide (DMF), *N*-methyl-2-pyrrolidone (NMP), dimethyl sulfoxide (DMSO),

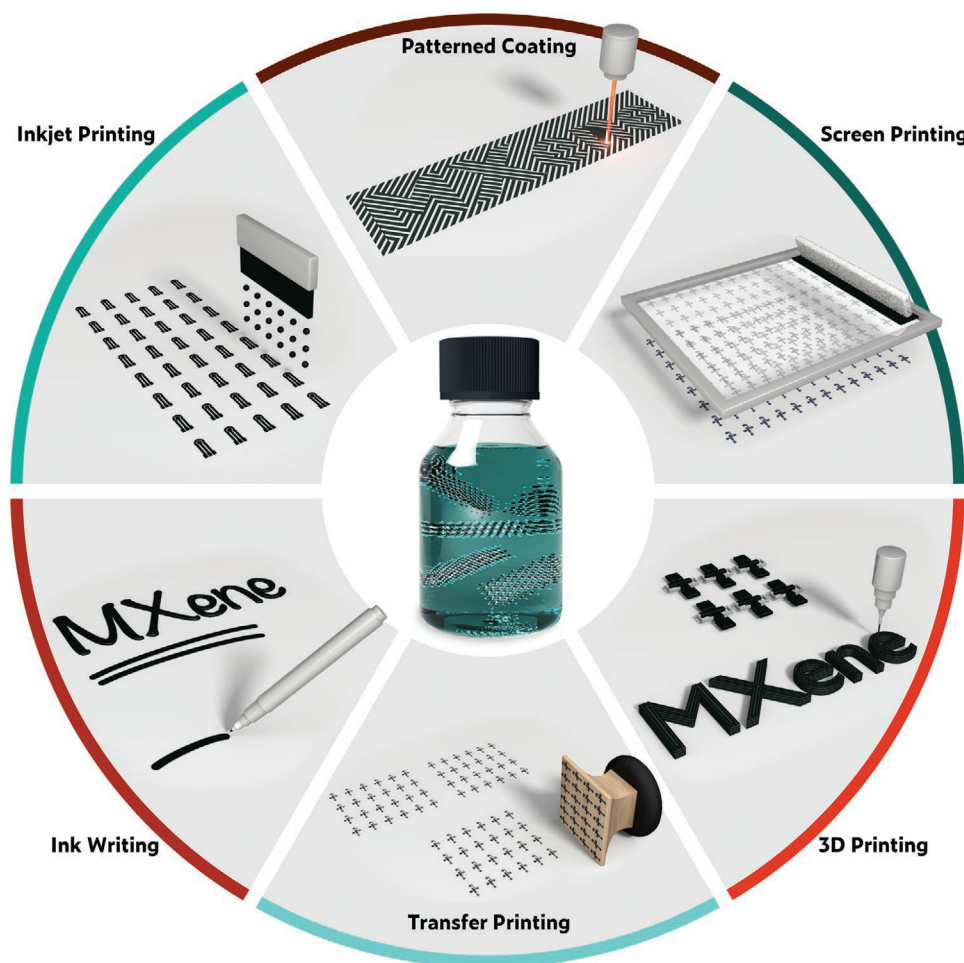


Figure 4. The main printing/coating techniques to prepare patterned MXene films. Clockwise: screen printing, 3D printing, transfer printing, ink writing, inkjet printing, and patterned coating represented by laser patterning of a pre-formed MXene film.

propylene carbonate (PC), and ethanol,^[45] more importantly, MXene flakes dispersed in these solvents show much better stability against oxidation when compared with those dispersed in water, this is because the solvation shells of the organic molecules serve as protection layers against oxidation. In particular, the concentration of the dispersed MXene and solvent viscosity show a linear relationship with PC, NMP, and DMSO, meaning a smooth flow of the inks when these solvents are chosen for various printing techniques. More insights about the MXene-solvent interaction were obtained by examining the absorbance per path length (A/l), and plotting the A/l versus the Hildebrand parameter and fitting to a Gaussian, from which Kathleen et al. found that a peak located at $\approx 27 \text{ MPa}^{1/2}$, matching the previous result that PC is a good solvent. The result also predicts the excellent dispersion of $\text{Ti}_3\text{C}_2\text{T}_x$ in other solvents with a similar cohesion energy density.

3. Introduction to Printing and Coating Methods

For practical applications, it is necessary to be able to deposit patterned solid-state MXene films with a thickness of nanometers to micrometers starting from MXene colloidal dispersions.

Different printing/coating techniques have been reported to achieve this objective (Figure 4).^[56–60] Depending on whether a template is used, printing techniques can be divided into digital printing such as inkjet printing and 3D printing, and nondigital printing such as screen and transfer printing.^[17] Apart from these traditional printing methods, there are also a variety of coating techniques, such as Meyer rod coating, spray coating, vacuum filtration coupled with patterning approaches such as masking and laser patterning, that are used for obtaining different MXene patterns out of its dispersion. These different printing/coating techniques differ in ink fluidic properties, resolution and scalability. So far, inkjet printing, screen printing, and extrusion type 3D printing are the main methods used for printing MXene.

3.1. Inkjet Printing

As a noncontact, digital, and high-resolution technique, inkjet printing has been widely used to fabricate various devices like transistors,^[61] photosensors,^[62] and energy storage devices.^[63–65] Drop-on-demand (DOD) inkjet printers based on the piezoelectric and thermal mechanism are the most commonly used

inkjet printers for laboratory-scale research. The piezoelectric inkjet printers utilize the electric field to create pressure that can push ink out of a nozzle into individual droplets toward the substrate. While the thermal-type printer works by heating the resistive elements to form bubbles which can eject ink onto the substrate.

Preparing printable inks with suitable physical fluidic properties is the major challenge for inkjet printing. The inverse Ohnesorge number Z is often used to characterize the fluidic properties and ink printability,^[66] which is defined as

$$Z = \frac{(\alpha\rho\gamma)^{1/2}}{\eta} \quad (5)$$

where α is the printer nozzle diameter, ρ is fluidic density, γ is the surface tension, and η is the fluidic viscosity. The optimal Z range suggested by Jang et al. for inkjet-printable ink is between 4 to 14.^[67] However, Zhang et al. demonstrated printable MXene inks in different organic solvents with the Z value of around 2.6 for ethanol ink, about 2.5 for dimethyl sulfoxide (DMSO) ink and approximately 2.2 for NMP inks.^[56] Wang et al. reported a stable inkjet printing process with the Z value of 19 for water-based MnO₂ nanosheets ink with Triton X-100 surfactant and propylene glycol additives,^[65] whereas printable glycol-water and photoresist ink with the low Z value of 1 was reported by Hsiao et al.^[68]

Another issue is the wetting of printed patterns with substrates. Hu et al. suggested the ink surface tension should be lower than the substrate surface energy of 7–10 mN m⁻¹.^[69] Ink formulation engineering is required to achieve proper wetting and uniform deposition of materials. On the other hand, substrate treatment is an alternative strategy to facilitate ink wetting on the substrate. By using AlO_x-coated polyethylene terephthalate (PET) substrate (γ about 66 mN m⁻¹), MXene ink in DMF (37.1 mN m⁻¹), NMP (40.8 mN m⁻¹) and DMSO (43.5 mN m⁻¹) could be inkjet-printed on flexible PET substrate.^[56]

The advantages of inkjet printing include: 1) the digital deposition process without using a mask, which facilitates printing of complicated patterns. 2) Various substrates such as rigid silicon substrate, flexible polymer substrates, and even commercial paper substrates can be used for printing. 3) The high resolution shows promise for the fabrication of micrometer-scale devices. Inkjet printing mainly has two drawbacks: 1) It is challenging to prepare printable formulations with suitable rheological properties. 2) Preparing printable inks with suitable physical fluidic and morphological properties is difficult.

3.2. Screen Printing

Different from inkjet printing, screen printing works by depositing materials through squeezing high-viscosity inks through a stencil screen onto substrates. Flat-bed and rotary approach are the two main screen printing modes. More specifically, the flat-bed method works by pressing the ink through a flat patterned screen onto a substrate followed by repeating this process to achieve multilayer deposition; while the rotary approach works by pressing inks through a polyester screen cylinder and perforated metal onto a substrate. The rheological behavior

of MXene inks plays a crucial role in screen printing. For example, monolayer MXene ink shows a viscosity of 288.2 Pa s at a shear rate of 0.1 s⁻¹.^[70] By increasing the shear rate, the viscosity decreases linearly, suggesting an ideal non-Newtonian fluid property which enables the continuous screen printing of MXene ink through the screen mesh. The storage modulus (G') and loss modulus (G'') as a function of oscillation strain were used to characterize the rheological properties of the ink further. The solid-like behavior ($G' > G''$) before the yield point enables the solidification of the ink during the printing process. On the other hand, the liquid-like behavior ($G'' > G'$) after yield point shows viscous characteristics that enable smooth printing at high shear stresses. In another example, the viscosity of the nitrogen-doped MXene ink was also found to decrease with increasing shear rate, indicating shear-thinning non-Newtonian fluid behavior.^[57] The high viscosity at the initial shear rate enables high-resolution printed patterns without short-circuiting. Furthermore, the elastic behavior ($G' > G''$) was found at low shear stress (<100 Pa), suggesting solid-like behavior, which is beneficial for solidification of the ink during the screen printing process. While at high shear stress (>500 Pa), the ink shows liquid-like behavior due to the dominating G'' . This behavior enables the ink to be smoothly extruded through the screen mesh to the substrate at high shear stresses, while still retaining the printed structure after the printing process.

The advantages of screen-printing include: 1) Thick printed patterns with high aspect ratio and easily tunable thickness. 2) Low-cost and mass-printing. On the other hand, high-viscosity inks, low resolution, and high roughness are the main drawbacks of screen-printing.

3.3. Transfer Printing

Transfer printing means transferring material from relief features on an intermediate medium onto the target substrate, it enables heterogeneous integration of different classes of materials into desired layouts, and have found great application in flexible/stretchable electronics.^[71] Transfer printing using a polymeric stamp is common in the laboratory. However, gravure and flexographic transfer printing hold the greatest promise for scaled production. Gravure printing refers to the process of using gravure rollers to transfer the designed pattern pre-engraved into the gravure roller onto the substrate under pressure. The gravure printing system consists of an ink trough and a metal doctor blade which scrapes the excess ink from the roller surface. To achieve ink transfer, the substrate is passed between the gravure roller and the impression roller. Flexographic printing deposits ink by transferring the ink applied to the surface of screened roller cylinder onto the sacrificial support substrate followed by removing the excess ink from the non-image area by a doctor blade, ensuring an even spreading of ink on the anilox roller, and the remaining ink passes to the flexo plate, where it finally deposits onto the substrate. Differences between gravure and flexographic transfer printing are the applied pressure and ink transfer pathway.^[72] Apart from these, the printing speed (around 1000 m min⁻¹ for gravure and 500 m min⁻¹ for flexographic), as well as the ink viscosity (100–1000 mPa s for gravure printing, 50–500 mPa s for

flexographic printing), are also different.^[4] To make effective deposition by transfer printing, the adhesion between interfaces of ink/donor/substrate needs to be carefully optimized. The advantages of gravure and flexographic transfer printing are high printing speed and high scalability. The main drawbacks are the high cost of setting up and prototyping of gravure rollers and plates, as well as high volume requirements for inks.

3.4. Pen-Based Direct Ink Writing

Pen-based direct ink writing methods work by using daily writing tools such as fountain pens and rollerball pens to deposit inks of desired materials, and have shown great promise for the low-cost and convenient fabrication of electronics and energy storage devices.^[73] Due to the resolution difference between writing tools, e.g., 50–500 μm for brush pen and 100–800 μm for rollerball pen, coupled with the different wetting properties of substrates, patterns with different resolution can be readily obtained for different applications. However, an appropriate writing tool should be carefully selected for a specific ink and substrate to achieve smooth patterning. The limited resolution is an apparent drawback for pen-based direct ink writing. Moreover, the varied writing force by hand could lead to nonuniform and irreproducible deposition of materials on the substrate. Nevertheless, direct ink writing is still a promising method for low-cost, fast, and lab-scale fabrication and testing of electronics. One more advantage for direct ink writing is the less strict requirement on physical fluidic properties for inks, thus making the technique suitable for a wide range of dispersions based on functional materials.

3.5. 3D Printing

Additive manufacturing (AM) or 3D printing refers to the process of fabricating complex 3D architectures in a digital way. Different from subtractive manufacturing, AM fabricates the desired objects with designed structures without wasting materials. Light-based and ink-based are the two main modes for 3D printing.^[74] Light-based 3D printing methods including stereolithography and selective laser sintering exhibit high resolution but are limited in printing speed and printable materials. Photopolymerizable resins or thermoplastic polymer powders are normally used for light-based 3D printing. On the other hand, ink-based 3D printing methods, including fused deposition modeling (FDM), binder jetting, and DIW of soft materials are the main printing approach for laboratory-scale fabrication. These methods can be used to print a wide range of materials. FDM is the main mechanism behind most desktop 3D printers currently present on the market. It works by extrusion of filaments through a hot printhead followed by solidification through cooling upon deposition on the substrate. Therefore, the printable materials for FDM are only limited to thermoplastic polymers like polylactic acid. Thus, the most useful ink-based 3D printing method for the purpose of printing novel, noncommercialized materials is direct ink writing, which works by extrusion of shear-thinning viscoelastic materials.^[75] Typical viscosity value for DIW is in the range

of 10^2 – 10^6 mPa s.^[74] Recently, Zettl and co-workers demonstrated 3D printing of MXene by interfacial assembling $\text{Ti}_3\text{C}_2\text{T}_x$ nanosheets with amine-terminated ligands (*n*-butylamine) at the oil-water interface.^[76] Negatively charged MXene inks with controlled flow rates were extruded by a 3D printer into a high-viscosity silicon oil-ligand matrix. After printing, the oil-water interface was populated with MXene with a 3D filament-like structure. In fact, the high-concentration MXene aqueous dispersion obtained from the delamination step of the routine MXene synthesis, sometimes also known as MXene paste, can be directly used for 3D extrusion printing.^[56] The fast-drying property of water makes solidification easy, thus enabling the fast printing process.

3D printing presents several advantages including 1) good control over the thickness and geometry of printed patterns, 2) outstanding printing flexibility, and 3) cost-effectiveness and environmental friendliness. The limited choice of printable materials is the main drawback of 3D printing.

3.6. Patterned Coating

Although printing has great advantages in terms of resolution, scalability and pattern complexity, it sometimes poses stringent requirements on equipment and more importantly on the rheological and morphological properties of inks, thus materials that can be printed are limited, not to mention the complex procedures required to formulate materials into printable inks. In this regard, traditional coating methods (e.g., drop-casting, spin coating, bar coating, spray coating, vacuum filtration, etc.) are advantageous for material testing and device prototyping due to the less stringent requirements on equipment and ink properties. To date, several deposited MXene patterns have been achieved by utilizing any of the aforementioned traditional coating techniques, followed by patterning using a mask or laser cutting. Spray coating is a widely used deposition technique in art and industry; it works by applying pressure to a transporting gas to spray ink through a nozzle where an aerosol is formed.^[77] Spray coating allows fast and thin (from nm to μm range) uniform coating over a large area; however, the uniformity can be difficult to obtain as several parameters including solvent, flow rate, the distance between substrate and nozzle, substrate temperature all affect the obtained film properties. Rod coating is one of the most common methods to deposit medium-thick (μm) films and holds great potential for up-scaling.^[78] Vacuum filtration is also widely used in the lab to obtain free-standing films of 2D nanomaterials with μm thickness. It is a useful method to make composite films; however, the transfer of the film from the membrane to other substrate or to be a free-standing film can be difficult. In terms of patterning, metal, or polymer (e.g., polyimide) masks are usually used to assist coating. Various laser sources have also been used to pattern the MXene films after coating; however, the heat produced by the laser could lead to partial oxidation of the MXene on edges of the pattern.^[79] Compared with printing methods, patterned coating methods are much less demanding in the facility, and are thus less expensive; however, they are much more difficult to achieve controllable and precise patterning in terms of pattern complexity, tunable thickness, and surface roughness.

4. Printing MXenes for Various Applications

4.1. Energy Storage

MXenes possess high electrical conductivity and allow easy ion intercalation between layers, leading to excellent performance as electrodes for electrochemical capacitors (supercapacitors)^[80] and various kinds of batteries^[81–85]. However, the present reports on printing MXenes for energy storage nearly all focus on supercapacitors, with few studies on the lithium-ion battery.

Supercapacitors are a major type of energy storage device, bridging the gap between capacitors and batteries, characterized by virtue of their long cycle life and high power density. The two main charge storage mechanisms in electrochemical capacitors are electric double-layer capacitance and pseudocapacitance, in which surface redox reactions account for the charge transfer.^[86–89] MXenes predominately rely on pseudocapacitance as the charge storage mechanism, which, when coupled with the high electrical conductivity, endows MXenes with high volumetric capacitance.^[22] The recent reports on printed MXene-based supercapacitors are summarized in **Table 1**.

Zhang et al. reported additive-free MXene inks for inkjet printing and extrusion printing of microsupercapacitors (MSCs) recently (**Figure 5a**).^[56] Both aqueous and nonaqueous inks have been demonstrated for extrusion printing. The aqueous inks were prepared by dispersing $\text{Ti}_3\text{C}_2\text{T}_x$ nanosheets in DI-water while the organic inks were prepared by dispersing $\text{Ti}_3\text{C}_2\text{T}_x$ nanosheets in organic solvents including NMP, DMSO, DMF, and ethanol. The inverse Ohnesorge Z numbers were about 2.6 for ethanol ink and about 2.2 for NMP ink, which falls within the optimal Z range required for stable inkjet printing.^[16] As shown in **Figure 5b**, the inkjet-printed lines of the NMP and ethanol inks exhibited high resolution without the “coffee-ring” effect. Moreover, the inkjet-printed MXene lines from organic inks showed homogenous surface with interconnected nanosheet network. The sheet resistance of the inkjet-printed $\text{Ti}_3\text{C}_2\text{T}_x$ lines decreased from $445 \, \Omega \, \text{sq}^{-1}$ (printed layer number $\langle N \rangle = 1$) to $35 \, \Omega \, \text{sq}^{-1}$ ($\langle N \rangle = 50$). Meanwhile, the printed lines exhibited an electronic conductivity as high as $2770 \, \text{S cm}^{-1}$ which decreased to $1093 \, \text{S cm}^{-1}$ after 1000 bending cycles. High concentration ink (around $36 \, \text{mg mL}^{-1}$) with viscosity of around $0.7 \, \text{Pa s}$ was prepared for extrusion printing. The printed patterns showed continuous features consisting of interconnected $\text{Ti}_3\text{C}_2\text{T}_x$ nanosheets. The printed MSCs with two printed paths showed high resolution with a line gap of around $120 \, \mu\text{m}$ and a line width of around $438 \, \mu\text{m}$ on the porous paper substrate (**Figure 5c**). Due to the high concentration of the aqueous inks for extrusion printing, the sheet resistance of the extrusion-printed line decreased from 2000 to $10 \, \Omega \, \text{sq}^{-1}$ with an increasing printed layer number from 1 to 5. Less printing path can improve production efficiency and will thus benefit practical industry applications. Since ideal inks should exhibit high concentration (C) and high electronic conductivity (σ) to achieve optimized production efficiency, $\text{FoM} = \sigma C \, (\text{S cm}^{-1} \, \text{mg mL}^{-1})$ can be used to characterize the quality of inks. As shown in **Figure 5d**, the prepared MXene ink delivered the highest FoM value of $66\,996 \, (\text{S cm}^{-1} \, \text{mg mL}^{-1})$ compared to other printable inks like graphene, carbon nanotubes, and poly(3,4-ethylenedioxythiophene) polystyrene sulfonate. Both inkjet printing and

extrusion printing were used to fabricate all-MXene MSCs with poly(vinyl alcohol, PVA)/sulfuric acid (H_2SO_4) gel electrolyte. The cyclic voltammetry (CV) curves with rectangular shape suggesting pseudocapacitive behavior of printed MSCs. As shown in **Figure 5e**, the inkjet-printed MSC using the NMP-based $\text{Ti}_3\text{C}_2\text{T}_x$ ink showed specific areal capacitance as high as $12 \, \text{mF cm}^{-2}$ and specific volumetric capacitance of $562 \, \text{F cm}^{-3}$ when $\langle N \rangle = 25$, while only showed a capacitance of $1.3 \, \text{mF cm}^{-2}$ at $\langle N \rangle = 2$, showing the enhancement of areal capacitance due to the increase in printed layer number. The extrusion-printed MSC exhibited specific areal capacitance of $43 \, \text{mF cm}^{-2}$ with $\langle N \rangle = 5$. It showed energy density of $0.32 \, \mu\text{Wh cm}^{-2}$ at a power density of $11.4 \, \mu\text{W cm}^{-2}$ and maintained $0.11 \, \mu\text{Wh cm}^{-2}$ at a high power density of $158 \, \mu\text{W cm}^{-2}$ which are an order of magnitude higher than most printed MSCs. Furthermore, both printed MSCs exhibited excellent cycling performance with capacitance retention of around 100% and 97% for inkjet-printed and extrusion-printed MSCs, respectively.

The low stability of nanosheets in aqueous media limits the development of printing MXenes. To overcome this limitation, Wu et al. reported an aqueous MXene ink with excellent oxidation resistance by capping $\text{Ti}_3\text{C}_2\text{T}_x$ nanosheets with sodium ascorbate (SA).^[90] The as-prepared SA-MXene with various ligands exhibited high dispersity and stability over 80 days in water. Apart from protection by ligand, the mild reducing strength of ascorbate also contributes to the stabilization of MXene. As shown in **Figure 5f**, sodium ascorbate exhibits the best protective ability compared to the other agents like glucose, glutathione, oxalic acid, sodium borohydride, and hydrazine. Among them, strong reducing agents like sodium borohydride caused significant aggregation of $\text{Ti}_3\text{C}_2\text{T}_x$ nanosheets after 5 days. In-plane interdigitated electrodes were fabricated by inkjet printing SA-MXene ink as electrodes on paper followed by drop-casting PVA/ H_2SO_4 gel electrolyte on top. The printed MSC showed areal capacitance of $108.1 \, \text{mF cm}^{-2}$ and volumetric capacitance of $720.7 \, \text{F cm}^{-3}$, indicating the promise of highly stable ligand-capped MXene inks for printed energy storage applications.

Beyond inkjet printing, screen printing was also used to fabricate MXene-based supercapacitors. Xu et al. demonstrated a coplanar asymmetric microscale hybrid device (MHD) using $\text{Ti}_3\text{C}_2\text{T}_x$ nanosheets as a negative electrode and Co-Al layered double hydroxide (LDH) nanosheets as a positive electrode (**Figure 6a,b**).^[91] Co-Al LDH nanosheets were screen-printed on Au current collector followed by screen printing the $\text{Ti}_3\text{C}_2\text{T}_x$ nanosheets ink. PVA/KOH gel electrolyte was drop-cast onto the device to complete the device fabrication process. To fabricate asymmetric MHD, $\text{Ti}_3\text{C}_2\text{T}_x$ nanosheets and Co-Al LDH nanosheets were studied in three-electrode measurements first. $\text{Ti}_3\text{C}_2\text{T}_x$ electrode exhibited a quasi-rectangular shape owing to the intercalation of Li^+ and H_2O molecules between $\text{Ti}_3\text{C}_2\text{T}_x$ nanosheets, leading to fast diffusion and intercalation of electrolyte ions. Co-Al LDH electrode showed broad oxidation/reduction peaks with moderate peak separation, suggesting a redox behavior close to the pseudocapacitive behavior (**Figure 6c**). The potential window of MHD in $6 \, \text{M KOH}$ could extend to $1.45 \, \text{V}$ without oxygen evolution, showing the large working potential window of the as-prepared asymmetric MSC. The all-solid-state asymmetric MHDs reached a specific capacitance of

Table 1. Recent works on printed MXene-based supercapacitors.

Electrode materials	Configuration	Electrolyte	Electrochemical performance	Fabrication methods	Ref.
Ti ₃ C ₂ T _x	Symmetric, planar	PVA/H ₂ SO ₄	The areal capacitance of 12 mF cm ⁻² with printed 25 layers	Inkjet printing	[56]
Sodium ascorbate-Ti ₃ C ₂ T _x	Symmetric, planar	PVA/H ₂ SO ₄	The areal capacitance of 108.1 mF cm ⁻² and volumetric capacitance of 720.7 F cm ⁻³ , the volumetric energy density of 100.2 mWh cm ⁻³ at a power density of 1.9 W cm ⁻³	Inkjet printing	[90]
Ti ₃ C ₂ T _x (negative electrode)/ Co-Al LDH (positive electrode)	Asymmetric, planar	PVA/KOH	Areal capacitance of 28.5 mF cm ⁻² at a current density of 0.75 mA cm ⁻² , and areal energy density of 8.84 μWh cm ⁻²	Screen printing	[91]
RuO ₂ ·xH ₂ O@ Ti ₃ C ₂ T _x -Ag NWs	Symmetric, planar	PVA/KOH	Volumetric capacitance of 864.2 F cm ⁻³ at 1 mV s ⁻¹ , volumetric energy density of 13.5 mWh cm ⁻³ at power density of 48.5 W cm ⁻³	Screen printing	[70]
Nitrogen-doped Ti ₃ C ₂ T _x	Symmetric, planar	PVA/H ₂ SO ₄	Areal capacitance of 70.1 mF cm ⁻² at 10 mV s ⁻¹	Screen printing	[57]
Ti ₃ C ₂ T _x /Ti ₃ CNT _x	Symmetric, planar	PVA/H ₂ SO ₄	Areal capacitance of 61 mF cm ⁻² at 25 μA cm ⁻² , areal energy density of 0.76 μWh cm ⁻² at 0.33 mW cm ⁻²	Transfer/stamp printing	[58]
Ti ₃ C ₂ T _x	Symmetric, planar	PVA/H ₂ SO ₄	Areal capacitance of 43 mF cm ⁻² , areal energy density of 0.32 μWh cm ⁻² at 11.4 μW cm ⁻²	Extrusion printing	[56]
Ti ₃ C ₂ T _x	Symmetric, planar	PVA/H ₂ SO ₄	Areal capacitance of 2.1 F cm ⁻² at 1.7 mA cm ⁻² and gravimetric capacitance of 242.5 F g ⁻¹ at 0.2 A g ⁻¹ , areal energy density of 0.0244 mWh cm ⁻² at 0.64 mW cm ⁻²	3D printing	[54]
Ti ₃ C ₂ T _x	Symmetric, planar	PVA/H ₂ SO ₄	Areal capacitance of 1035 mF cm ⁻² at 2 mV s ⁻¹ , areal energy density of 51.7 μWh cm ⁻²	3D printing	[28]
Nitrogen-doped Ti ₃ C ₂ T _x , CNT, GO and AC	Symmetric, planar	PVA/H ₂ SO ₄	the areal energy density of 0.42 mWh cm ⁻² at the areal capacitance of 8.2 F cm ⁻²	3D printing	[57]
Ti ₃ C ₂ T _x	Symmetric, planar	PVA/H ₂ SO ₄	The areal capacitance of 5 mF cm ⁻²	Pen-based direct ink writing	[59]
Ti ₃ C ₂ T _x , acetylene black and polyvinylidene fluoride	Symmetric, coplanar	PVA/H ₂ SO ₄	The energy density of 0.77 μWh cm ⁻² at a power density of 46.6 mW cm ⁻²	Meyer rod coating and laser patterning	[79]
Ti ₃ C ₂ T _x (positive electrodes)/ carbon or zinc (negative electrodes)	Asymmetric, planar	PVA/Zn(CF ₃ SO ₃) ₂	Areal capacitance of 66.5 mF cm ⁻² at current density of 1 mA cm ⁻²	Laser patterning	[93]
Ti ₃ C ₂ T _x with bacterial cellulose fiber	Symmetric, planar	PVA/H ₂ SO ₄	The areal capacitance of 111.5 mF cm ⁻² at a current density of 2 mA cm ⁻²	Vacuum filtration with laser patterning	[94]
Ti ₃ C ₂ T _x	Symmetric, planar	PVA/H ₂ SO ₄	The areal capacitance of around 27 mF cm ⁻² and volumetric capacitance of about 357 F cm ⁻³ at 20 mV s ⁻¹ , Volumetric energy density between 11 and 18 mWh cm ⁻³ with a power density of 0.7–15 W cm ⁻³	Spray coating	[60]
Ti ₃ C ₂ T _x	Symmetric, planar	PVA/H ₂ SO ₄	The areal capacitance of 23.4 mF cm ⁻²	Spray coating and laser patterning	[95]

28.5 mF cm⁻² at a current density of 0.75 mA cm⁻². Furthermore, all-solid-state MHD exhibited excellent capacitance retention of 92% after 10 000 cycles. To demonstrate the practical application of MHD in portable electronics, the asymmetric MHDs were integrated with the force sensor on PET and paper substrates. As shown in Figure 6d, the weak vibration of the arteries in fingers was detected, indicating the potential of screen-printed asymmetric MHDs as power units for portable electronic devices.

Li et al. reported the fabrication of flexible MSC by screen printing RuO₂@ Ti₃C₂T_x nanosheets with silver nanowires (AgNWs) as electrodes materials.^[70] The hydrous RuO₂

nanoparticles which were decorated onto the surface of MXene have strong van der Waals interaction or chemical interactions with the residual oxygen-containing functional groups on the surface of MXene flakes. As illustrated in Figure 6e, the RuO₂@ Ti₃C₂T_x-AgNWs ink was screen-printed onto a paper substrate with an interdigitated structure followed by drop-casting PVA/KOH gel electrolyte onto the device. Due to the presence of the AgNWs network for rapid charge transfer, the screen-printed electrode exhibited conductivity as high as 17 800 S cm⁻¹, which is higher than that of the MXene ink (12 182 S cm⁻¹). For comparison, MXene ink, MXene and AgNWs ink (M-A ink), nano-composite ink containing RuO₂·xH₂O nanoparticles,

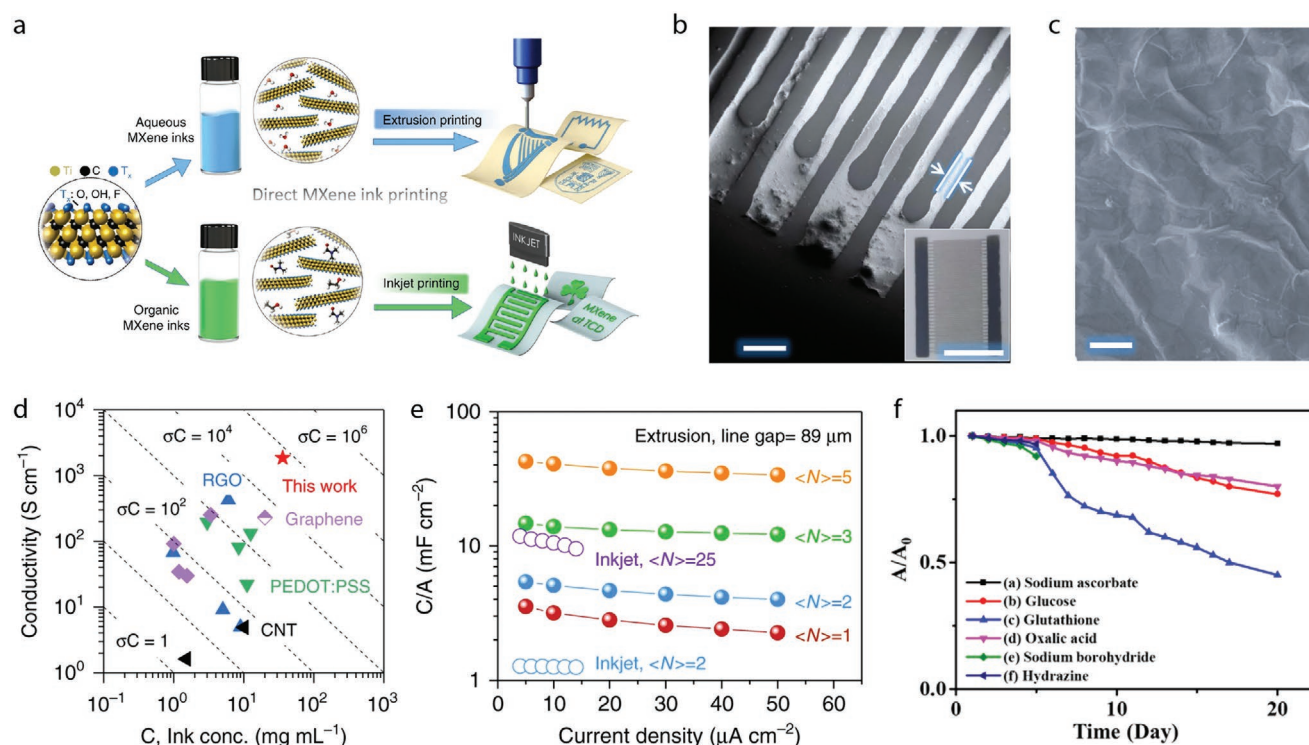


Figure 5. a) Schematic illustration of inkjet and extrusion printable MXene inks. b, c) SEM images of inkjet-printed MSC by NMP-based ink (b) and extrusion-printed MSC on paper (c). Scale bar in (b) and (c) are 200 μm and 500 nm, respectively. d) Comparison of the conductivity and ink concentration of the printed lines. e) The areal capacitance of inkjet- and extrusion-printed MSCs with different printed layer number (N). a–d) Reproduced with permission.^[56] Copyright 2019, Springer Nature. f) Time course of the relative absorbance (A/A_0) at 800 nm of the pristine MXene (without ligands) colloid suspension in the presence of different agents. Reproduced with permission.^[90] Copyright 2019, Elsevier Ltd.

MXene, and AgNWs ink (R@M-A0.75:1 ink) were prepared for screen printing MSCs with PVA/KOH gel electrolyte. As shown in Figure 6f, all four different MSCs exhibited symmetrical rectangular shapes without peaks at 100 mV s^{-1} , indicating ideal capacitive behavior owing to the surface absorption of electrolyte ions and the continuous reversible redox reactions on the surface of MXene nanosheets. The incorporation of AgNWs into MXene could enhance the electrical conductivity resulting in a high current response than pure MXene MSC. Moreover, the introduction of $\text{RuO}_2 \cdot x\text{H}_2\text{O}$ nanoparticles further increased the capacitance of devices because of the additional pseudocapacitance from RuO_2 in alkaline electrolyte. More specifically, R@M-A0.75:1 MSC exhibited the largest current response suggesting the highest charge storage capability. The printed R@M-A0.75:1 MSC showed a high volumetric capacitance of 864.2 F cm^{-3} at 1 mV s^{-1} , which maintained 340.0 F cm^{-3} at a scan rate of 2000 mV s^{-1} . Moreover, the devices showed excellent cycling performance with 90% capacitance retention after 10 000 cycles at a scan rate of 100 mV s^{-1} . Furthermore, the screen-printed MSC exhibited excellent mechanical flexibility with about 87.3% capacitance retention after 2000 bending cycles with 5.0% bending strain, showing promise as a power unit for flexible electronics.

In another example, Yu et al. reported the printing of nitrogen-doped MXene (N-MXene) nanosheets as electrodes for symmetric supercapacitors.^[57] N-MXene nanosheets were

prepared by adding a melamine-formaldehyde template into the MXene dispersion, followed by annealing in Ar ambient to produce N-doped MXene. The high-angle annular dark field image and elemental mapping demonstrated the homogenous distribution of Ti, C, and N elements and the uniform N doping into the $\text{Ti}_3\text{C}_2\text{T}_x$ nanosheets (Figure 6g). The high-resolution X-ray photoelectron spectroscopy (XPS) spectrum in Figure 6h showed three peaks at 454.7, 455.7, and 457.8 eV, which could be assigned to Ti–C, Ti–N, and Ti–O bonding, respectively. The Ti–N peak further confirmed that C atoms in $\text{Ti}_3\text{C}_2\text{T}_x$ nanosheets were substituted by N atoms. The electrical conductivity and electrochemical performance of N-doped $\text{Ti}_3\text{C}_2\text{T}_x$ nanosheets were enhanced through surface modification. The screen-printed MSC with N-doped $\text{Ti}_3\text{C}_2\text{T}_x$ nanosheets electrodes and PVA/ H_2SO_4 gel electrolyte delivered areal capacitance as high as 70.1 mF cm^{-2} at 10 mV s^{-1} which was higher than pure MXene MSC (13.8 mF cm^{-2} at 10 mV s^{-1}). Transfer/stamp printing has also been demonstrated as a low-cost and scalable technique to fabricate MXene-based supercapacitors. Recently, Zhang et al. demonstrated using a stamping strategy to deposit $\text{Ti}_3\text{C}_2\text{T}_x$ and Ti_3CNT_x inks on a flexible substrate to build all-MXene MSCs.^[58] The designed stamps were 3D-printed, then MXene inks were transferred onto them (Figure 7a). $\text{Ti}_3\text{C}_2\text{T}_x$ inks with a high concentration of 22 mg mL^{-1} and high viscosity (around 1.37 Pa s) were prepared for stamping, as shown in Figure 7b. Stamp-printed MXene film on paper substrate maintained high conductivity (resistance

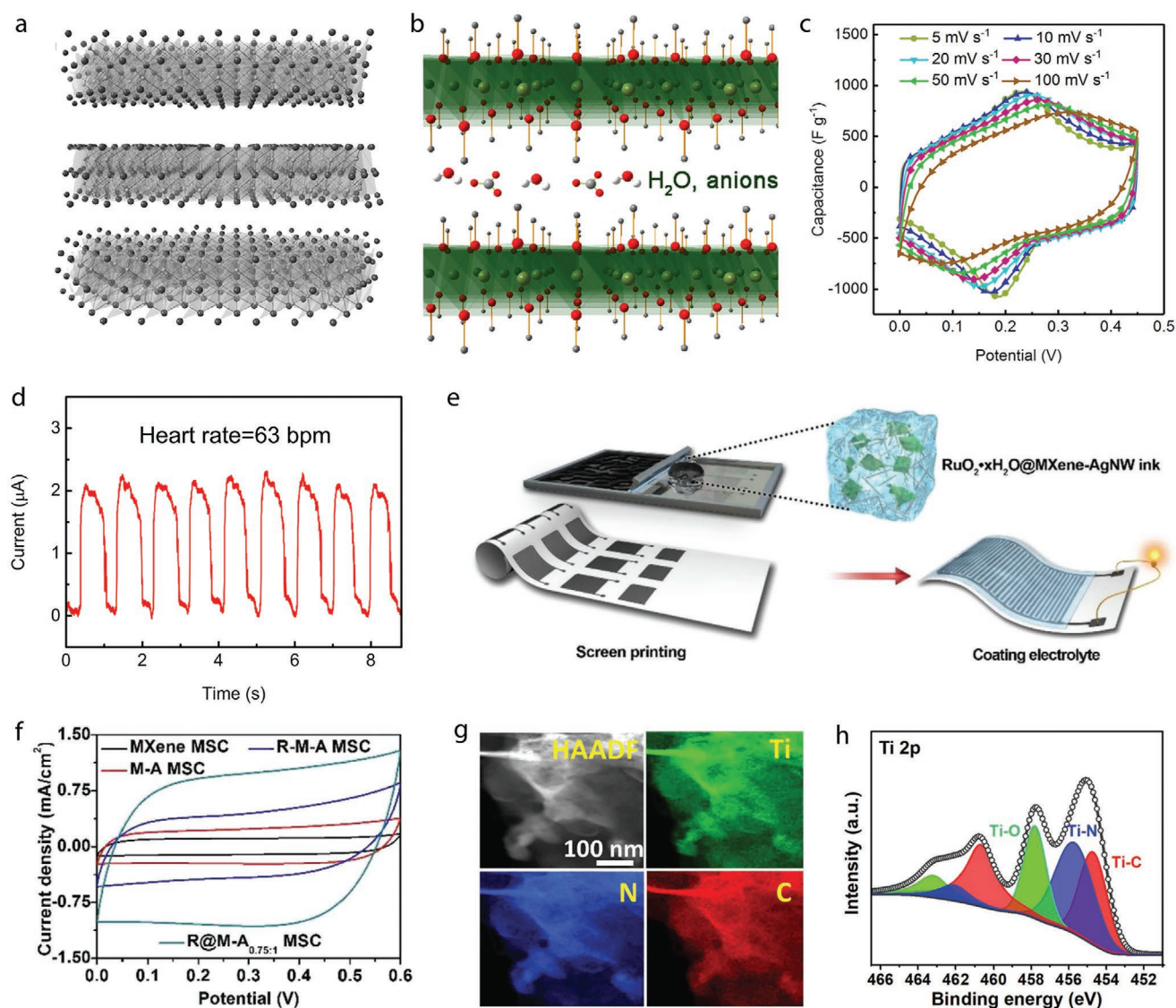


Figure 6. a,b) Schematic of the $\text{Ti}_3\text{C}_2\text{Tx}$ (a) and Co-Al-LDH (b) structures. c) CVs at different scan rates for the Co-Al-LDH electrode in 6 M KOH. d) The measured live heartbeat waveform showing the heart rate of about 63 bpm. a–d) Reproduced with permission.^[91] Copyright 2018, Elsevier Ltd. e) Schematic illustration of screen-printed flexible MSC. f) The CV of four configurations of MXene-based MSCs at a scan rate of 100 mV s^{-1} . e,f) Reproduced with permission.^[70] Copyright 2019, Wiley-VCH. g) Scanning transmission electron microscopy image and elemental maps of N-doped MXene. h) High-resolution XPS spectrum of Ti 2p of N-doped MXene. g,h) Reproduced with permission.^[57] Copyright 2019, Wiley-VCH.

changes <15%) after repeated bending/releasing cycles, demonstrating the high flexibility and high conductivity of the stamped MXene films. Flexible stamped MXene MSCs with different configurations on the paper substrate were investigated to optimize the device structures. As shown in Figure 7c, decreasing the interspace of electrodes resulted in a high areal capacitance of 57 mF cm^{-2} at a scan rate of 5 mV s^{-1} . Increasing electrode finger numbers have also improved the device performance due to the increased active sites for energy storage. The optimized interdigitated $\text{Ti}_3\text{C}_2\text{Tx}$ MSCs showed areal capacitance as high as 61 mF cm^{-2} at a current density of 25 $\mu\text{A cm}^{-2}$. Furthermore, the stamped MSC exhibited good cycling stability and flexibility with 85% capacitance retention after 1600 bending cycles (Figure 7d).

To achieve maximum surface area accessibility and ion transport, Yang et al. reported using extrusion 3D printing to fabricate 3D $\text{Ti}_3\text{C}_2\text{Tx}$ electrodes for supercapacitors.^[54] First, additive-free MXene inks with suitable rheological properties were developed, then the ink was printed on top of the substrate followed by freeze-drying resulting in a 3D architecture without further thermal or chemical treatment. Different architectures were successfully printed using 3D printable MXene ink, as shown in Figure 8a. The 3D-printed structures exhibited distinct filament shapes without internal collapse, indicating the suitability of the additive-free MXene inks for 3D printing (Figure 8b). MSCs were fabricated by 3D printing MXene inks with tunable electrodes thickness and PVA/ H_2SO_4 gel electrolyte. The 3D-printed MSC with a high mass loading of

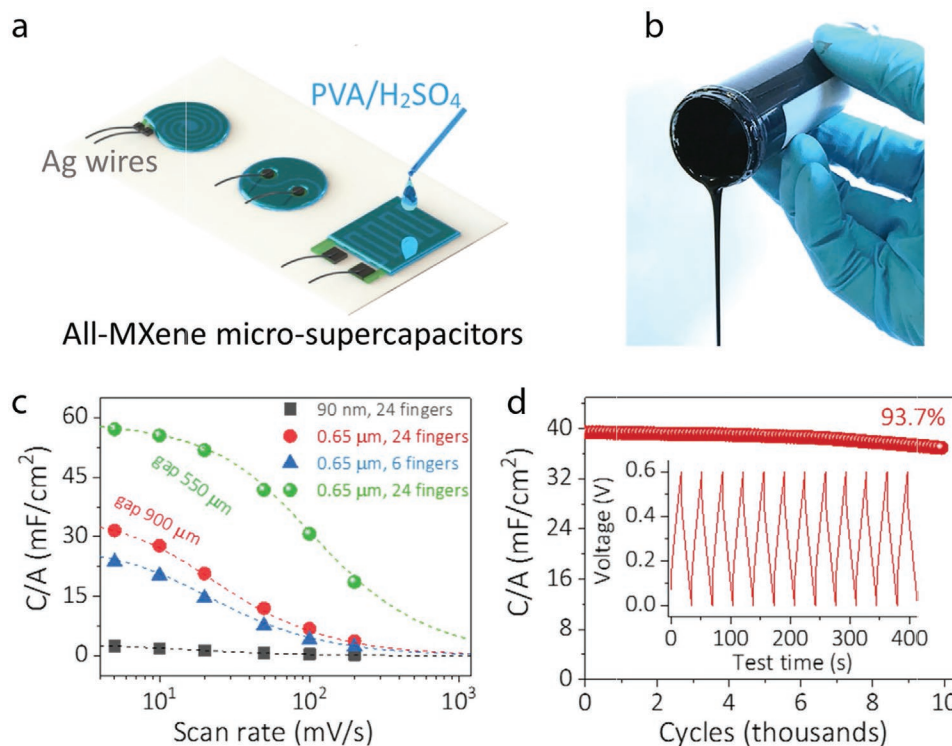


Figure 7. a) Schematic illustration of stamp-printed supercapacitors. b) Optical images of $\text{Ti}_3\text{C}_2\text{T}_x$ inks. c) Areal capacitances of $\text{I-Ti}_3\text{C}_2\text{T}_x$ with various configurations. d) Long-term cycling stability of the MXene MSC. a–d) Reproduced with permission.^[58] Copyright 2018, Wiley-VCH.

8.5 mg cm^{-2} without a short circuit was obtained. The CV curve of the MSC exhibited a quasi-rectangular shape suggesting typical capacitive characteristics (Figure 8c). The 3D-printed MSC achieved high areal capacitance of 2.1 F cm^{-2} at a current density of 1.7 mA cm^{-2} and showed excellent cycling stability with 90% capacitance retention after 10 000 cycles (tested at 1 A g^{-1}). Moreover, the device delivered a high energy density of $0.0244 \text{ mWh cm}^{-2}$ at a power density of 0.64 mW cm^{-2} . To improve the electrochemical performance of the $\text{Ti}_3\text{C}_2\text{T}_x$ electrodes, Yu et al. demonstrated a 3D extrusion printable composite ink based on nitrogen-doped MXene nanosheets, active carbon, carbon nanotube and graphene oxide (Figure 8d).^[57] Various architectures like the “MXENE” scaffold can be made by 3D extrusion printing, as shown in Figure 8e. The 3D printed electrodes were used to build symmetric SCs, which achieved a high areal energy density of 0.42 mWh cm^{-2} at the areal capacitance of 8.2 F cm^{-2} . Beidaghi and co-workers also demonstrated the fabrication of MSCs with high energy density by 3D printing of additive-free $\text{Ti}_3\text{C}_2\text{T}_x$ nanosheets as electrodes (Figure 8f).^[28] Due to the viscoelastic properties of MXene ink, the printed electrodes with multiple layers showed good mechanical stability without collapsing (Figure 8g). Moreover, the cross-sectional scanning electron microscopic (SEM) images show the highly horizontal alignment of MXene nanosheets in the 3D printed electrodes because of the alignment of MXene nanosheets in the nozzle during extrusion and shear alignment in the nozzle movement direction during printing. The horizontally aligned MXene electrode is crucial for the movement of electrolyte ions in MSC with an interdigitated structure. The 3D printed solid-state MSC with PVA/ H_2SO_4 gel electrolyte

exhibited areal capacitance as high as 1035 mF cm^{-2} and a high energy density of 57.1 μWh cm^{-2} .

Compared with the above printing techniques, direct writing techniques using daily writing tools show great promise for the facile deposition of materials on various substrates. Quain et al. demonstrated that direct writing of additive-free MXene water-based ink for energy storage applications.^[59] $\text{Ti}_3\text{C}_2\text{T}_x$ nanosheets ink with a high concentration of 30 mg mL^{-1} and optimal viscosity was developed and loaded into the cartridge of a rollerball pen without any leaking or clogging (Figure 9a). As shown in Figure 9b, the prepared MXene ink can be deposited onto the paper substrate smoothly by direct writing. The resistance of the written lines on paper decreased from $40 \text{ k}\Omega$ (single line) to $0.1 \text{ k}\Omega$ (multiple overlapping lines). Due to the capillary effect of cellulose fibers,^[92] the ink could completely fill the pores of paper, resulting in a continuously conducting coating. To prove the potential of direct writing for energy storage applications, current collector-free MSCs were fabricated by directly writing MXene ink on the paper substrate. PVA/ H_2SO_4 gel electrolyte was used to complete the MSC fabrication. It is notable that direct writing enables fast and single-step fabrication of in-plane MSCs on different substrates with easy patterning capability. Due to the high electron conductivity of MXene, the printed MSC exhibited rectangular CV curves indicating ideal capacitive behavior.^[35] The MSC reached a high areal capacitance of 5 mF cm^{-2} . While being convenient, direct writing is not a perfect technique to fabricate large scale MXene patterns. To achieve this, Alshareef and co-workers used a scalable, low-cost and straightforward laser-based method to “write” MXene patterns on a MXene paper coated by using a Meyer rod followed by

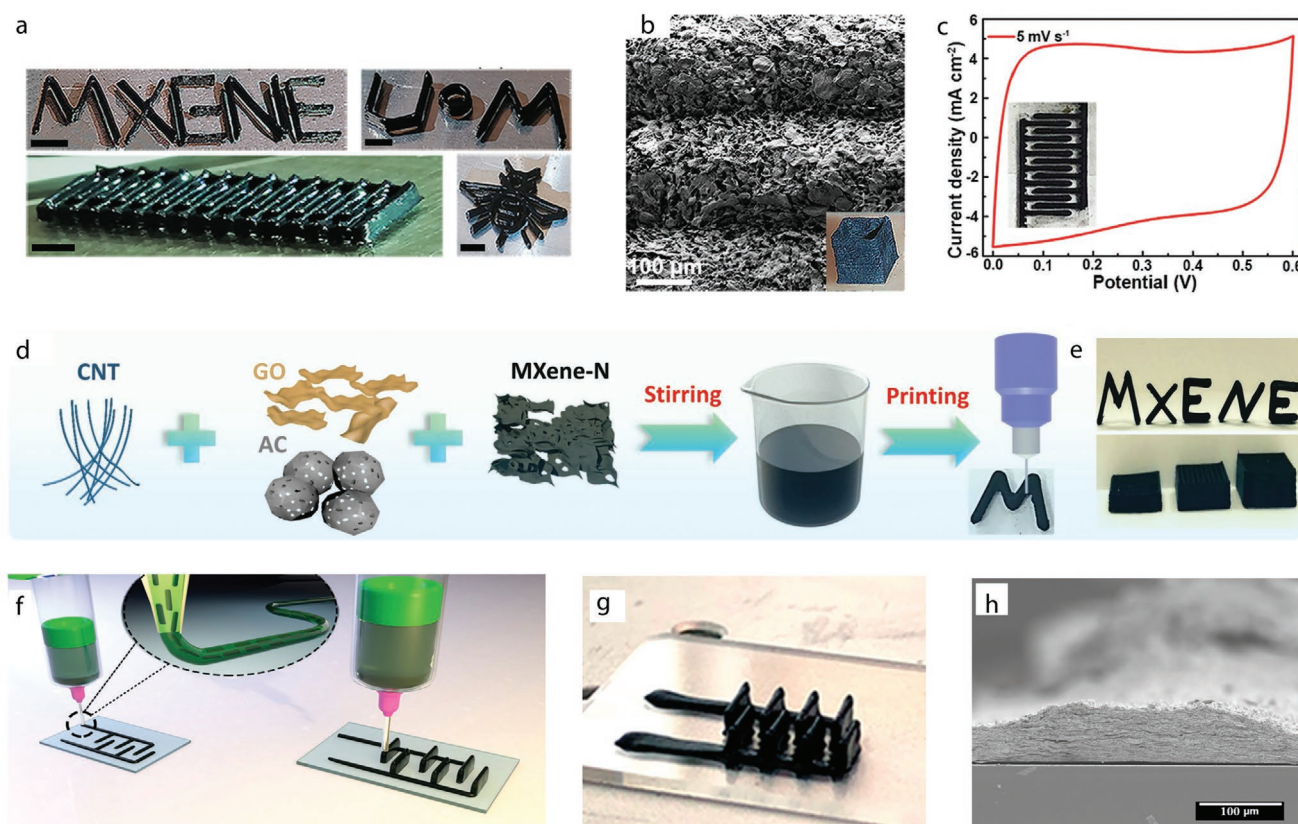


Figure 8. a) Illustration of 3D-printed architectures. b) SEM and optical photographs (inset) of a hollow rectangular prism. c) The CV of 3D-printed MSC at 5 mV s⁻¹. Inset is the optical image of 3D-printed MSC with MXene interdigitated electrode configuration. a–c) Reproduced with permission.^[54] Copyright 2019, Wiley-VCH. d) Schematic illustration of 3D printing of designed patterns. e) Optical images of 3D-printed patterns. d,e) Reproduced with permission.^[57] Copyright 2019, Wiley-VCH. f) Schematic illustration of 3D printing MSCs. g) Optical image of 3D printed MSC on a glass substrate. h) Cross-sectional SEM image of the printed electrode. f–h) Reproduce with permission.^[28] Copyright 2020, American Chemical Society.

laser patterning.^[79] As shown in Figure 9c, a MXene slurry containing Ti₃C₂T_x nanosheets, acetylene black and poly(vinylidene fluoride) was coated on paper by the Meyer rod coating technique to obtain uniform film over the entire paper surface. Due to the capillary action of cellulose fibers, the adhesion between MXene and paper substrate was enhanced, resulting in conformal coating and excellent adherence. To make paper-based MSCs, a laser was used to pattern the MXene-coated paper into an interdigitated structure (Figure 9d). The electrochemical performance of the fabricated MSC was tested in both 1 M H₂SO₄ aqueous electrolyte and PVA/H₂SO₄ gel electrolyte. The as-prepared MSC exhibited areal capacitance of 25 mF cm⁻² at a scan rate of 20 mV s⁻¹ in 1 M H₂SO₄ electrolyte and delivered an energy density of 0.77 μWh cm⁻² at a power density of 46.6 mW cm⁻² in PVA/H₂SO₄ gel electrolyte (Figure 9e).

To increase the voltage window, building asymmetric SCs and using ionic liquid electrolytes are promising approaches. Wang et al. fabricated asymmetric MSCs with MXene as positive electrodes and porous carbon or Zinc as negative electrodes.^[93] As shown in Figure 9f, MXene slurry was coated on both sides of Ni foil by blade coating followed by UV laser cutting into a predesigned interdigital structure; then polyimide adhesive tapes were pasted to fix and connect the edges of electrodes; lastly, PVA/LiCl gel electrolyte was coated on electrodes.

To fabricate asymmetric MSCs, two pieces of Ni foils were used as the current collector to cover both the positive electrode (MXene slurry) and the negative electrode (Zn). Then UV laser was utilized to pattern the two sets of finger electrodes, followed by assembling onto plastic substrate and coating with PVA/Zn(CF₃SO₃)₂ electrolyte. This asymmetric MSC can be charged to 1.1 V and achieved areal capacitance of 66.5 mF cm⁻² at a current density of 1 mA cm⁻². Moreover, the asymmetric MSC showed excellent mechanical performance.

To be used as a power source for flexible and stretchable electronics, flexible MSCs with high mechanical flexibility and excellent electrochemical performance under repeated tensile deformation are required. Jiao et al. reported stretchable MSCs based on freestanding MXene/bacterial cellulose composites paper electrodes.^[94] Ti₃C₂T_x nanosheets/bacterial cellulose hybrid dispersion was vacuum filtrated to get composite paper followed by magnetron sputtering of the Au layer on top to get freestanding and flexible Au/MXene/bacterial cellulose paper. To prepare patterned electrodes, laser-cutting was used to pattern the composite paper into kirigami patterns. PVA/H₂SO₄ gel electrolyte was drop cast on top of the device to complete the MSCs fabrication. The obtained MSC achieved areal capacitance as high as 111.5 mF cm⁻² at a current density of 2 mA cm⁻². The bacterial cellulose, which acted as glue linking

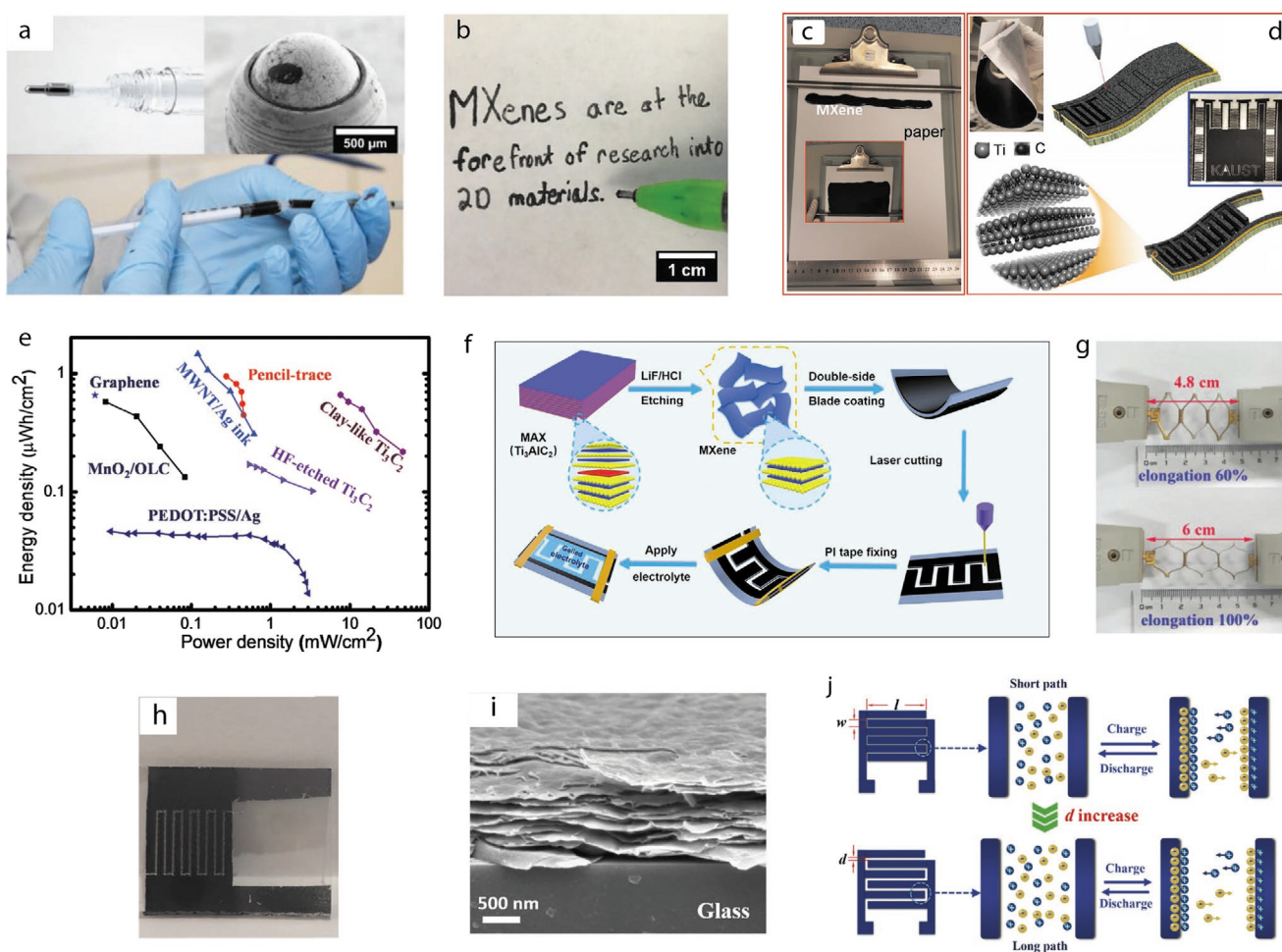


Figure 9. a) Images of the rollerball pen used for direct writing of Ti_3C_2 inks. b) Direct writing of MXene ink on the paper substrate. a,b) Reproduced with permission.^[59] Copyright 2019, Wiley-VCH. c) Meyer rod coating of MXene slurry on A4 paper. d) Schematic illustration of MXene-based paper supercapacitor made by rod coating followed by laser patterning. e) Ragone plot of the obtained MXene-based MSC. c–e) Reproduced with permission.^[79] Copyright 2016, Wiley-VCH. f) Illustration for the fabrication process of double-side MSCs. Reproduced with permission.^[93] Copyright 2019, Wiley-VCH. g) Optical images of MSC consisting of 4 MSC units connected in series under an applied strain at 60% and 100% elongation. Reproduced with permission.^[94] Copyright 2019, Wiley-VCH. h) Digital photograph showing an as-fabricated MSC on a glass substrate, about the size of a US dime. i) Cross-sectional SEM image of spray-coated $\text{Ti}_3\text{C}_2\text{Tx}$ film on the glass substrate. h,i) Adapted with permission.^[60] Copyright 2016, The Royal Society of Chemistry. j) Schematic illustration for the transport mechanism of electrolyte ions within the paper-based MSC with different interspaces. Reproduced with permission.^[95] Copyright 2019, Elsevier Ltd.

the nanosheets together, can significantly enhance the mechanical strength of the composite electrodes. Therefore, the MSCs showed high flexibility and stretchability from 0% to 100% elongation without noticeable deterioration in electrochemical performances (Figure 9g).

Different from vacuum filtration, spray coating can directly deposit materials on substrates without further transfer process. Peng et al. reported solid-state MXene MSCs by spray coating $\text{Ti}_3\text{C}_2\text{T}_x$ nanosheets as electrodes.^[60] First $\text{Ti}_3\text{C}_2\text{T}_x$ nanosheets with large lateral size were spray-coated on the glass substrate as the current collector, followed by spray coating small lateral-size $\text{Ti}_3\text{C}_2\text{T}_x$ nanosheets on top as the electroactive layer. Laser cutting was used to pattern the MXene film into an interdigitated structure. PVA/ H_2SO_4 gel electrolyte was employed to obtain all-solid-state MSCs (Figure 9h). The cross-sectional SEM in Figure 9i shows the

MXene nanosheets with a layer-by-layer structure that could facilitate the movement of electrolyte ions in in-plane MSCs. The obtained MSC achieved high areal capacitance of around 27 mF cm^{-2} and volumetric capacitance of about 357 F cm^{-3} at a scan rate of 20 mV s^{-1} . Moreover, the MSC delivered volumetric energy density values between 11 and 18 mWh cm^{-3} with a power density of $0.7\text{--}15 \text{ W cm}^{-3}$.

Paper has also been reported as a substrate for spray coating MXene inks to make MSCs. $\text{Ti}_3\text{C}_2\text{T}_x$ nanosheets were spray-coated onto paper as active materials and current collectors followed by UV laser cutting into interdigitated structures. PVA/ H_2SO_4 gel electrolyte was drop cast on top of the electrodes. Poly(dimethylsiloxane) (PDMS) glue was used to encapsulate the devices to build all-solid-state MSCs. Figure 9j illustrates the transport of ions in MSCs with different interfinger distance. Increasing the distance led to longer transport paths of

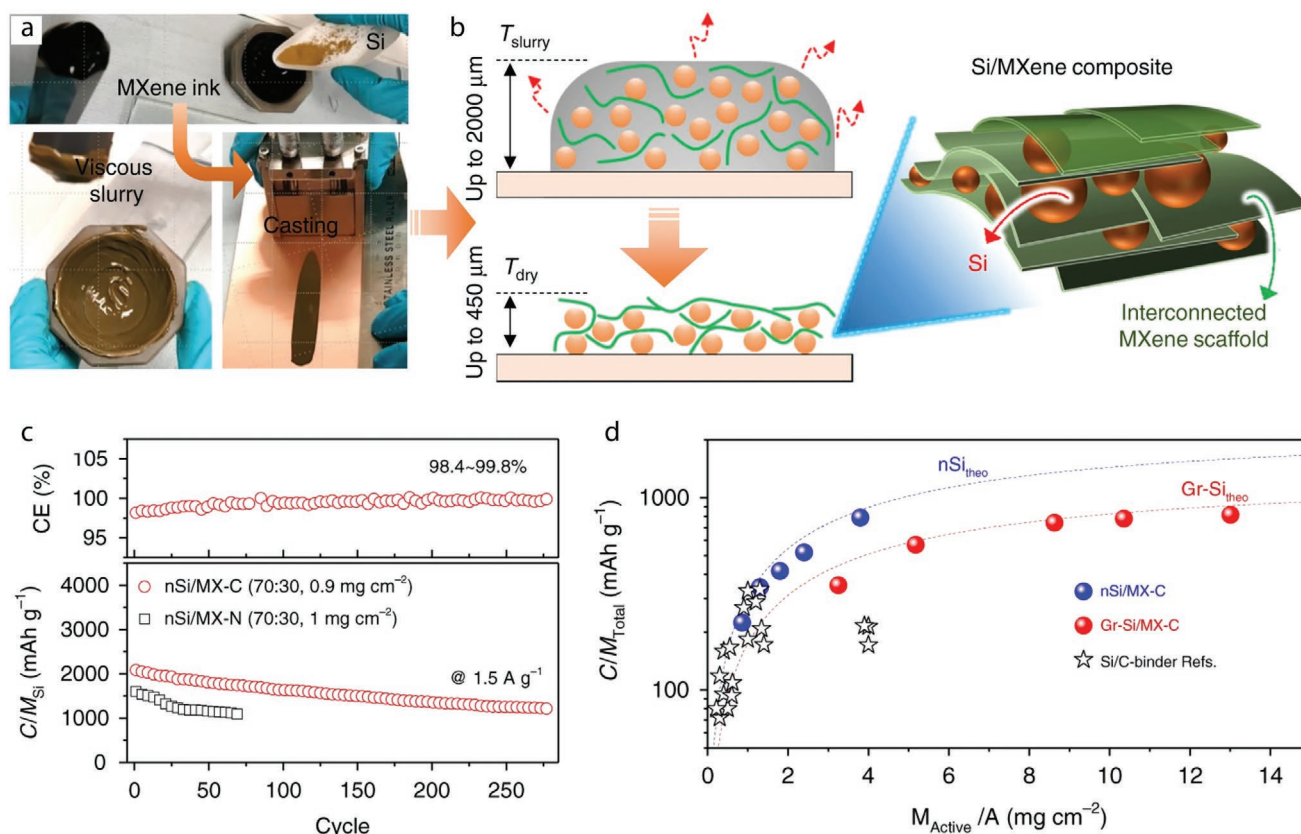


Figure 10. a,b) Fabrication of Si/MXene composite electrodes. c) Coulombic efficiency of nSi/MX-C (top), the lifetime of nSi/MX-C and nSi/MX-N electrodes at a rate of 1.5 A g^{-1} (bottom). d) Cell-specific capacity on the anode side plotted as a function of active materials mass loading and compared to the reported Si/C-binder systems. a–d) Reproduced with permission.^[97] Copyright 2019, Springer Nature.

electrolyte ions, which decreases the electrochemical performance of devices. The obtained paper-based MSC showed high areal capacitance of 23.4 mF cm^{-2} and excellent cycling stability of 92.4% capacitance retention after 5000 times cycling.

Batteries are the most widely used power source units for portable electronics applications. To satisfy the demand for flexible and wearable electronics, reliable and cost-effective batteries with high capacity, are urgently required. Much effort has been put into developing new electrode materials and electrolytes to improve capacity. On the other hand, novel fabrication approaches such as printing techniques can also be utilized to improve the electrochemical performance of batteries. Printing batteries show several advantages such as: a) easy fabrication of complex device architectures; b) precisely controlled shape and thickness of electrodes; c) low-cost, simple and scalable fabrication; d) promising for the manufacturing of all-solid-state batteries. Zhang et al. developed Si/ $\text{Ti}_3\text{C}_2\text{T}_x$ (MX-C) and Ti_3CNT_x (MX-N) inks to fabricate composite electrodes for lithium-ion batteries.^[96] To prepare their inks, nanoscale Si powders (nSi) and graphene-wrapped Si (Gr-Si) were mixed with MXene dispersion to form a homogenous and viscous slurry with proper rheological properties for coating on Cu foil without external binder or carbon black (Figure 10a). The thickness of the coated electrodes could reach 650 and 2100 μm for nSi and Gr-Si slurries, respectively, indicating high mass-loading. The evaporation process is illustrated in Figure 10b. MXene sheets were

deposited randomly after coating while forming continuous nanosheet networks wrapping Si nanoparticles. The nanosheet networks further developed a robust composite electrode with excellent mechanical properties. The electrode structure and thickness could be tuned by changing the concentration (or viscosity) of the MXene ink. The electrical conductivity plays a vital role in achieving high-performance batteries. Due to the excellent electrical conductivity of MXene nanosheets, adding 30% MXene into Si powder could enhance the conductivity of nSi/MX-C (3448 S m^{-1}), nSi/MX-N (336 S m^{-1}) and Gr-Si/MX-C (5333 S m^{-1}), respectively. Moreover, the composite electrodes maintained high electrical conductivity and excellent mechanical flexibility upon repeated bending, suggesting the potential for flexible and wearable electronics. The electrochemical performance of composite electrodes was studied. As shown in Figure 10c, the nSi/MX-C anode exhibits reasonable stability up to 280 cycle charge/discharge, which can be attributed to the synergistic effect between continuous MX-C sheets networks and Si particles. In addition, nSi/MX-C anode showed excellent Coulombic efficiency. However, the nSi/MX-N anode showed poor cycling stability compared with nSi/MX-C, which may be explained by the low fracture energy of nSi/MX-N anode, lower thermodynamic stability, and the less conductive MX-N sheets networks. The Gr-Si/MX-C anode was used to enhance the electrode mass loading and capacity further. Increasing mass fraction of MX-C in Gr-Si/MX-C anode could improve

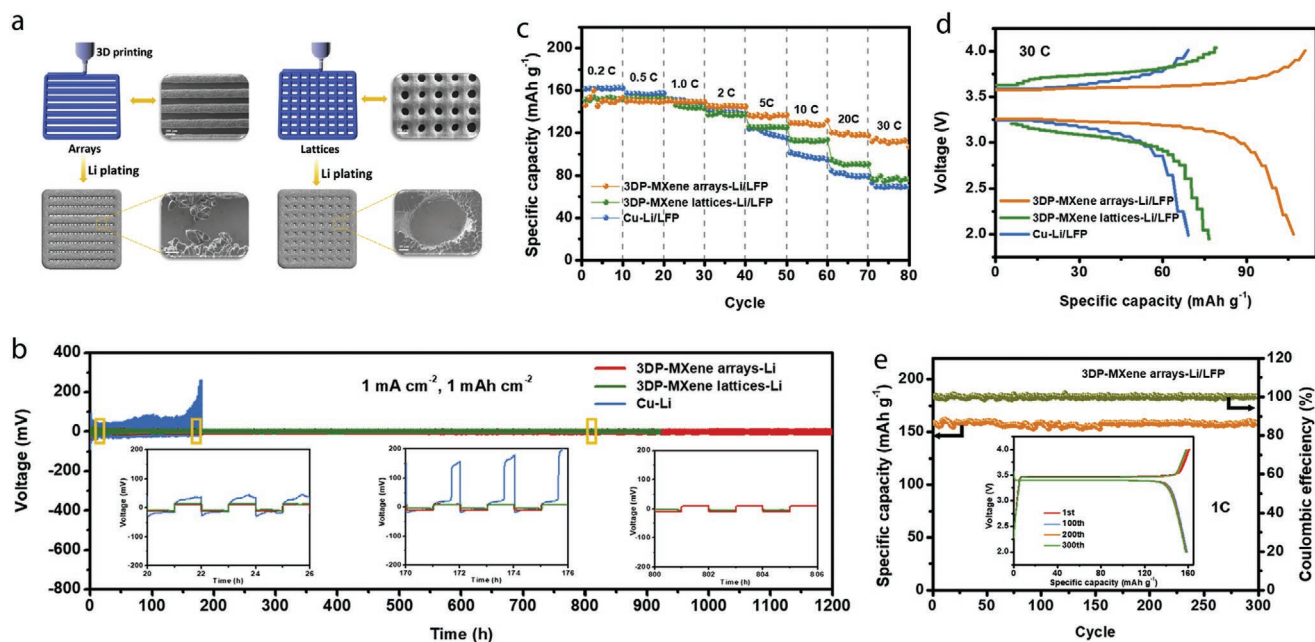


Figure 11. a) Schematic of the 3D printing process for MXene arrays and lattices to guide the nucleation and growth of lithium. b) Cycling performances of symmetric cells with 3DP-MXene arrays-Li, 3DP-MXene lattices-Li, and Cu-Li at 1 mA cm^{-2} , 1 mAh cm^{-2} . c) Rate capabilities of 3DP-MXene arrays-Li/LFP, 3DP-MXene lattices-Li/LFP, and Cu-Li/LFP. d) Charge-discharge profiles at 30 C. e) Cycling stability of 3DP-MXene arrays-Li/LFP. a–e) Reproduced with permission.^[98] Copyright 2019, Elsevier Ltd.

the anode capacity to the near theoretical value, and enhance the mechanical properties of the anode. Moreover, the cycling performance of the anode was dependent on the Gr-Si mass loading. Composite anodes were compared with reported Si/carbon binder systems. The mass of Cu foil, electrode, and half of the separator was taken into account to calculate the performance of composite electrodes. As shown in Figure 10d, nSi/MX-C and Gr-Si/MX-C electrodes showed higher capacity than the Si/C-binder systems on the cell level: nSi/MX-C and Gr-Si/MX-C electrodes delivered a capacity of 790 mAh g^{-1} at areal mass loading of 3.8 mg cm^{-2} and capacity of 815 mAh g^{-1} at areal mass loading 13 mg cm^{-2} , respectively, suggesting almost all Si active materials have been utilized.

Safety issue becomes a significant challenge for lithium-ion batteries nowadays because of the lithium dendrites growth leading to short-circuit. Shen et al. prepared a $\text{Ti}_3\text{C}_2\text{T}_x$ nanosheets ink with an ultrahigh concentration of about 300 mg mL^{-1} for printing MXene arrays with broad interspaces, showing the promise to inhibit the growth of lithium dendrites which could seriously compromise battery performances.^[98] The ink shows a shear-thinning behavior and high viscosity ($>102 \text{ Pa s}$), ideal for extrusion type 3D printing. The 3D-printed MXene arrays and lattices were used to guide the nucleation and growth of lithium. As shown in Figure 11a, cobblestone-like lithium was grown in 3D printed arrays with filament width of around $300 \mu\text{m}$ and interspace of about $200 \mu\text{m}$. However, lithium was grown around the hole walls in the 3D printed lattices. Nucleation overpotential of 3D printed arrays and lattices were measured at 0.5 mA cm^{-2} , which suggested a decrease in lithium plating barrier on MXene because of the large active nucleation sites of Ti–O–Li on the surface of MXene nanosheets. The symmetric cells were measured by

galvanostatic cycling to investigate the electrochemical performance of the 3D-printed MXene arrays and lattices. As shown in Figure 11b, pre-plated lithium on copper electrode exhibited higher overpotential than 3D-printed MXene arrays-Li and lattices-Li electrodes, owing to the nucleation function of $\text{Ti}_3\text{C}_2\text{T}_x$ nanosheets and uniform distributions of the lithium-ion flux and the electric field. The long-life cycle further demonstrates the high stability of 3D-printed MXene arrays-Li and lattices-Li electrodes. It is notable that the 3D-printed MXene arrays-Li are more stable than the 3D printed MXene lattices-Li. A full cell with LiFePO_4 cathode and 3D-printed MXene arrays-Li anode was assembled which exhibited high capacity of 149.4 mAh g^{-1} at 1C (Figure 11c), lower voltage hysteresis of the cell at high current rate 30C (Figure 11d) and excellent stability with 99.4% capacity retention after 300 cycles at 1C (Figure 11e).

4.2. Electronics and Optoelectronics

Owing to their vast compositional variation and tunable morphological/physicochemical characteristics, MXenes have garnered an immense potential in electronics. Although several semiconducting MXenes have been predicted and some have been synthesized, presently, the electronics community has been focusing on the metallic-like MXenes, exploring their applications in interconnects, antenna, electromagnetic interference (EMI) shielding, etc.^[24,99–101] On the other hand, MXenes have also exhibited intriguing optoelectronic and plasmonic properties owing to their ultra-broadband absorption, which almost spans the whole electromagnetic spectrum from UV-visible, near-infrared (NIR) and THz to radio-frequency.^[97,102–106] Nonetheless, their electronic and

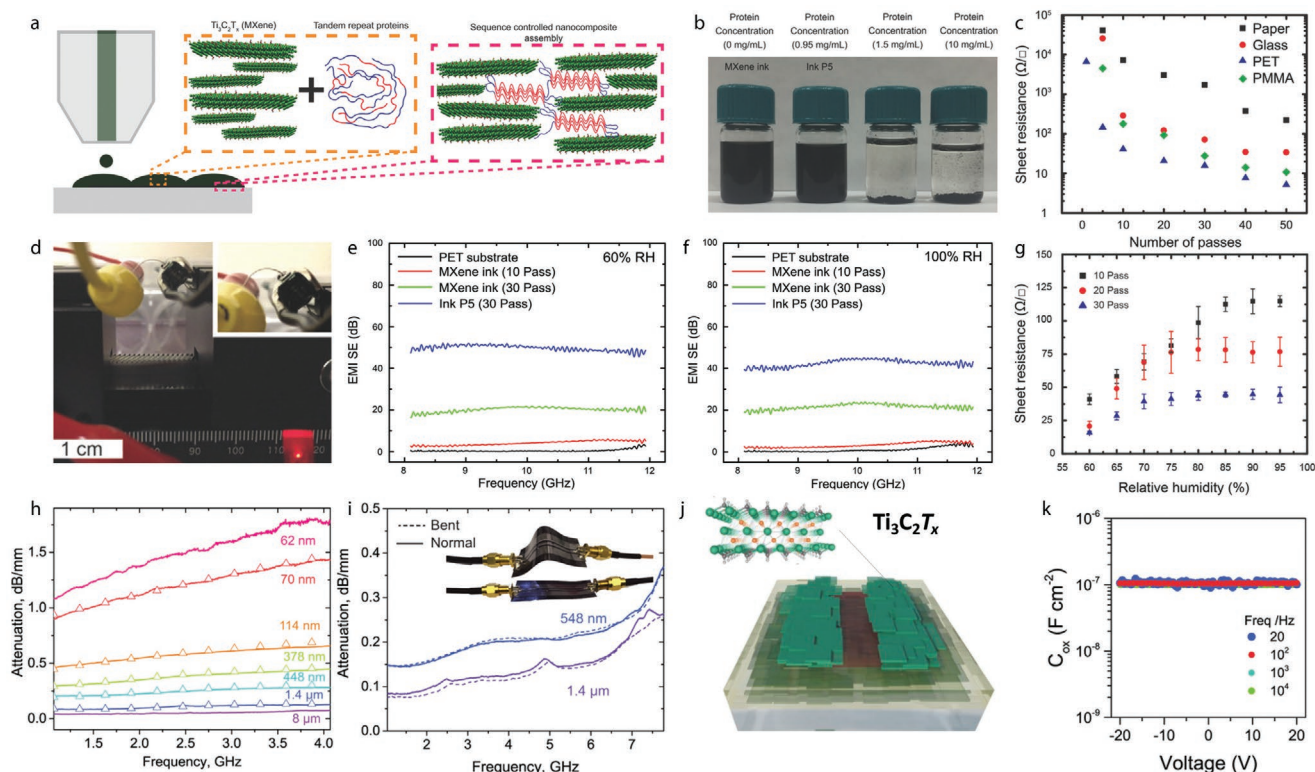


Figure 12. a) Schematic illustration of protein-mediated self-assembly of MXene nanosheets during the inkjet printing process. b) Pristine and different dispersions of protein-based MXene nanosheets in DMSO. c) Sheet resistance of inkjet-printed protein-based MXene films on different substrates. d) An LED circuit based on ink P5 inkjet-printed on flexible at bent state. Inset: the magnified image of the mechanically deformed film. e, f) PET EMI shielding efficiencies of large-area inkjet-printed MXene electrodes on PET at a relative humidity of 60% (e) and 100% (f). g) The sheet resistance of different ink P5 inkjet-printed on PET as a function of relative humidity. a–g) Reproduced with permission.^[107] Copyright 2018, Wiley-VCH. h) Thickness-dependent attenuation versus frequency obtained using different MXene waveguides. i) Attenuation as a function of the frequency of straight and bent MXene waveguides. Inset: Photographs of the MXene coplanar waveguide before and after bending. h, i) Reproduced with permission.^[102] Copyright 2018, American Association for the Advancement of Science. j) Schematic representation of all-MXene contacted TFTs. k) Capacitance–voltage (C–V) characteristics of the $\text{Ti}_3\text{C}_2\text{T}_x/\text{HfO}_2/\text{Ti}_3\text{C}_2\text{T}_x$ MIM capacitor using MXene as the source, drain and gate electrodes. j, k) Reproduced with permission.^[99] Copyright 2018, Wiley-VCH.

optical applications remain to be less than sufficient, and mostly limited to small-area devices. Hence, the well-controlled versatile patterning capability of printing is expected to promote the application of MXenes in electronics and optoelectronics greatly. However, only a few attempts have been made on this front so far.

Vural et al. inkjet printed $\text{Ti}_3\text{C}_2\text{T}_x$ MXene inks into large-area (≈ 2 cm) stimuli-responsive electrodes on various substrates including cellulose paper, glass, and flexible PET.^[107] To tackle the problems of poor jetting stability, and the formation of the “coffee ring effect” that results from the low viscosity of pure MXene ink, MXene nanosheets were dispersed in a high-viscosity solvent, i.e., DMSO with synthetic structural proteins as a binder (Figure 12a). The excellent dispersion quality of the MXene suspensions was preserved by limiting the concentration of the synthetic binders to 1 mg mL^{-1} , a value above which instant sheet aggregation started to take place (Figure 12b). The optimum dispersion quality of the protein-based MXene ink was obtained at a binder concentration of 0.95 mg mL^{-1} (named as ink P5 in this work). Those proteins can form hydrogen bonds with the 2D crystals of MXene, and thus could increase the jetting stability and film-forming quality of MXene inks.

During the inkjet printing process of the formulated MXene inks, either pristine or protein-based, the conductivity of the obtained films gradually increased as a function of printing cycles. For the optimum formulated MXene-based ink, i.e., ink P5, the conductivity of the corresponding inkjet-printed films on PET substrates was found to be as high as $\approx 1160 \text{ S cm}^{-1}$ with an average thickness of $\approx 2.25 \mu\text{m}$. It is worth mentioning that the obtained electrical conductivity of the printed MXene electrodes was almost 3–4 times higher than the inkjet-printed electrodes based on other 2D materials including graphene and reduced graphene oxide. The measured sheet resistance of the protein-based MXene ink (P5) inkjet-printed on different substrates is depicted in Figure 12c. To evaluate the performance of devices made of printed patterns based on the protein-containing MXene ink (P5) as well as the mechanical stability of the printed films, an LED circuit (Figure 12d) was assembled using the formulated P5 ink printed on PET substrate as electrodes. The printed electrodes were bent at different curvature radii while measuring the voltage passing through the LED circuit. Remarkably, the obtained voltage remained almost unaltered under the applied mechanical deformation, underlining the high mechanical stability of the printed protein-based MXene

electrodes. These results also highlight the protein-enhanced quality of adherence of the MXene nanosheets on PET flexible substrates. Furthermore, in addition to their demonstrated capability for flexible LED circuits, the inkjet-printed MXene electrodes were also evaluated for EMI shielding devices. The corresponding shielding efficiency (SE) of different MXene inks (pristine and protein-based) printed onto PET substrates, under dry conditions (i.e., 60% relative humidity), is displayed in Figure 12e. Apparently, as in the case of LED circuits, the addition of proteins to the MXene ink had also significantly increased the corresponding SE values by more than two-fold, marking the superiority of the protein-based MXene electrodes over their pristine counterparts. Moreover, the inclusion of protein also expanded the multifunctionality of the printed MXene films due to their sensitivity toward humidity. As shown in Figure 12f, the EMI SE of the P5-based printed electrodes has decreased by one-fold when subjected to wet conditions (100% relative humidity), while the pristine-based electrodes remained unchanged under the same conditions. This phenomenon was attributed to swelling of proteins induced by the humidity increase, leading to a rise in their volume, and thus a decrease in the volumetric fraction of the conductive MXene patterns (Figure 12g).

Sarycheva et al. have developed a patterning method based on an aqueous dispersion of $\text{Ti}_3\text{C}_2\text{T}_x$ MXene, demonstrating its application in the radio-frequency (RF) regime.^[102] The spray-coated MXene films were patterned to fabricate translucent flexible antenna, waveguides (Figure 12h), and RF identification device (RFID) tags. The performance of the fabricated MXene-based waveguides is highlighted here as an example of what patterning could add to the versatility of MXenes. The authors studied the dependence of the attenuation of different waveguides as a function of frequencies on the thickness of the patterned $\text{Ti}_3\text{C}_2\text{T}_x$ films (Figure 12i). The mechanical flexibility of the fabricated MXene-based waveguides is displayed in Figure 12j, showing that the obtained attenuation at two different thicknesses of unbent and bent MXene waveguides is almost identical. They have also demonstrated that both the RF antenna and waveguides could perform very well at thicknesses smaller than the skin depth of classical metals, i.e., copper (1.33 μm) and silver (1.29 μm) at 2.4 GHz. It is worth noting that such a remarkable performance was acquired by macro-patterning of MXene films, which underlines the significant potential that could be attained by high-resolution printing techniques. The above findings show the enormous potential of printed MXene-based products for the industry, particularly for wearable and flexible RF electronics.

Wang et al. have demonstrated an innovative patterning technique to fabricate all-MXene-contacted oxide thin-film transistors (TFTs) with n-type (ZnO) and p-type (SnO) channels.^[99] In this work, they spray-coated $\text{Ti}_3\text{C}_2\text{T}_x$ MXene film as a gate contact followed by the growth of the HfO_2 dielectric layer and an n-type or p-type channel. The MXene source and drain contacts were obtained by patterning the MXene film sprayed on the top using a well-designed lift-off technique to get the source and drain electrodes (Figure 12j). The capacitance-voltage characteristics of the $\text{Ti}_3\text{C}_2\text{T}_x/\text{HfO}_2/\text{Ti}_3\text{C}_2\text{T}_x$ metal/insulator/metal (MIM) capacitor are depicted in Figure 12k, showing an areal capacitance (C_{ox}) of $1.04 \times 10^{-7} \text{ F cm}^{-2}$. Both transistors, i.e.,

n-type and p-type, with MXene as the source, drain, and gate electrodes, have exhibited a balanced performance with field-effect mobility of 2.01 and 2.61 $\text{V}^{-1} \text{ s}^{-1}$, and switching ratio of 1.1×10^3 and 3.6×10^6 , respectively. Considering the simplicity of the lift-off patterning technique used in this work, significant performance improvement can be expected if well-designed printed patterns of MXene contacts were used.

In addition to electronics, the potential for a patterning-induced increase in the performance of optoelectronics has been recently demonstrated by Chaudhuri et al.^[106] In their work, pre-deposited $\text{Ti}_3\text{C}_2\text{T}_x$ MXene films ($\approx 400 \text{ nm}$ in thickness) were patterned using nanofabrication techniques (i.e., electron beam lithography and dry etching), to fabricate broadband plasmonic metamaterial absorbers (Figure 13a). The patterning quality of the nanopillars arrays is manifested by their corresponding SEM micrographs obtained at different incident angles (Figure 13b). The patterned arrays of MXene nanopillars have exhibited intense localized surface plasmon resonances at NIR frequencies. Figure 13c shows that the subwavelength-sized patterned structures have demonstrated a sizeable operational bandwidth with a higher absorption efficiency ($\approx 90\%$ at 1550 nm) compared to their nonpatterned counterparts ($\approx 30\%$ at the same wavelength). Such enhancement in the absorption cross-section of the patterned MXene films highlights the impact of patterning on the MXenes properties, opening the door for employing MXenes in a gamut of nanophotonic and nanoplasmonic applications. However, further efforts still need to be exerted to obtain large-area films with uniform high-resolution patterns, yet at low fabrication cost, which, again, underscores the necessity of exploring printing techniques for MXene-based optoelectronic devices.

Jiang et al. used inkjet printing to directly print MXene nanosheets in laser resonators, yielding a broadband ultrafast laser operations from NIR to mid-infrared (MIR) regions.^[108] By altering the inter-droplet distance, different patterns (e.g., dots, spaced and stacked stripes) based on a binder-free MXene ink were obtained (Figure 13d). Using a gold mirror as a substrate, different numbers of MXene layers have been printed, forming a saturable absorber (SA) device that can be integrated with different setups of laser resonators. An illustration of the stable ink ejection is depicted in Figure 13e, giving rise to an inkjet-printed MXene SA mirror with various printing layers (4 to 20 layers). MXene-printed gold mirrors (Figure 13f), in conjunction with different kinds of laser resonators (Figure 13g), have yielded ultrafast laser operations spanning the IR spectrum from 1 to 3 μm . As a result, a mode-locking operation was achieved within the telecommunication window, with a pulse duration of 100 fs. Such findings not only highlight the ultrafast broadband operations but also pave the way toward complicated laser integrations based on MXenes.

4.3. Sensing and Actuation

The unique property combination of hydrophilic surface and high electrical conductivity of $\text{Ti}_3\text{C}_2\text{T}_x$ MXene allows easy-fabrication of MXene-based sensors and actuators. The abundant surface functional groups of MXenes play an essential role

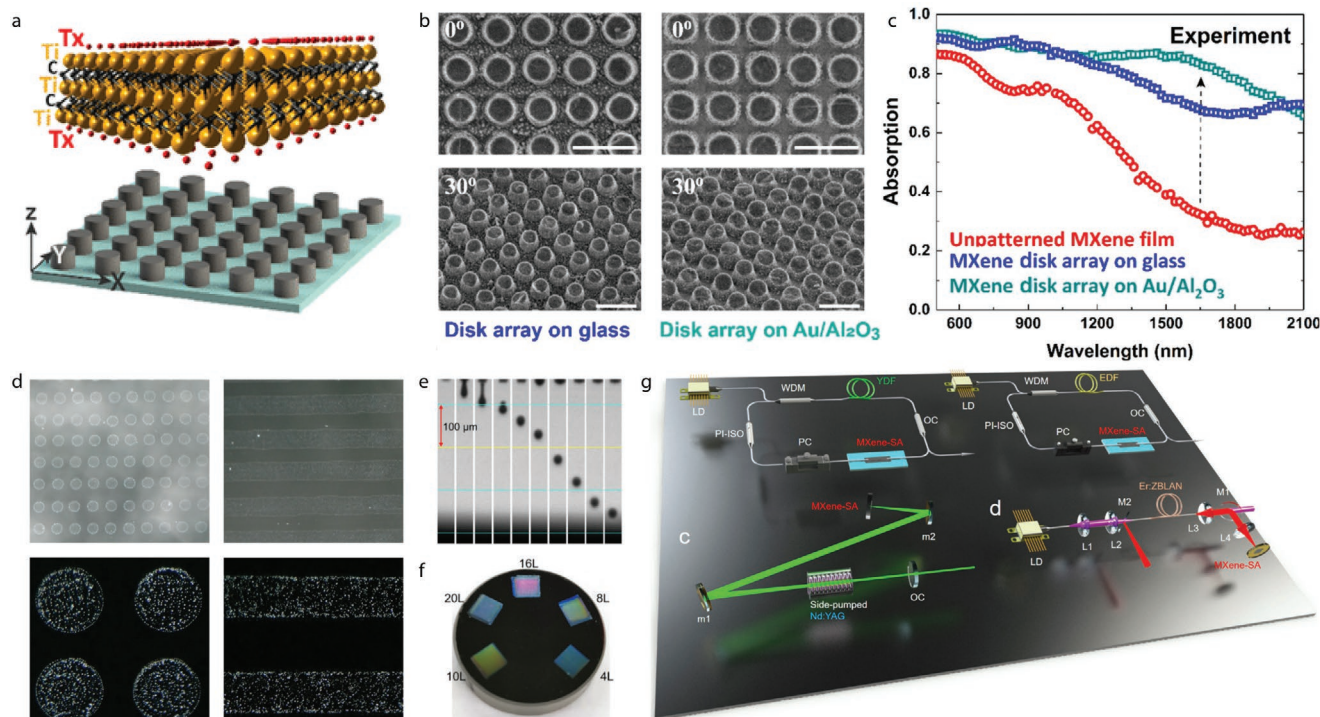


Figure 13. a) Schematic illustration of an array of patterned MXene nanopillars. b) SEM images, collected at different angles, for patterned MXene disk arrays on glass (left), and on Au/alumina (right). c) Experimental absorption spectra of the nonpatterned and patterned MXene films. a–c) Reproduced with permission.^[106] Copyright 2018, American Chemical Society. d) SEM images of printed arrays of $\text{Ti}_3\text{C}_2\text{Tx}$ dots and stripes on glass substrates. e) The stable ejected printing droplet sequences. f) Inkjet-printed MXene saturable absorber (SA) mirror with various printing layers (from 4 to 20). g) Schematic diagram of four different kinds (1–4) of laser resonators integrated with inkjet-printed MXene SA. d–g) Reproduced with permission.^[108] Copyright 2019, Springer Nature.

in the spontaneous interactions with other ions/molecules, making them useful in sensors.^[109–112] On the other hand, the combination of excellent electrical and thermal conductivity, as well as photothermal responsiveness, makes MXenes attractive candidates for high-performance actuators.^[113–115] In this part, we highlight the few examples of MXene-based printed sensors and actuators.

Ultrathin $\text{Ti}_3\text{C}_2\text{Tx}$ MXene micropatterns have been fabricated by a micro-contact printing method using aqueous MXene dispersion and PDMS stamp for bio-sensing application.^[116] (Figure 14a) The PDMS stamp was first treated by oxygen plasma for 5 minutes to enhance the hydrophilicity, then MXene dispersion was applied and dried under vacuum. MXene-coated PDMS stamp was gently placed onto a 3-aminopropyltriethoxysilane (APTES) treated clean glass coverslip for 3–5 minutes. After removal of the stamp, ultrathin MXene patterns with several layers were formed. The thickness of MXene strips was dependent on the concentration of MXene ink. Ultrathin MXene patterns with a thickness of ≈ 5 nm were used in this study to ensure enough electrical conductance and sensitive response to the target biomolecules (Figure 14b). The MXene micropatterns showed an ambipolar field-effect feature under electrolyte solution gating, and their p-type mode demonstrated a linear increase in conductance depending on the concentration of dopamine molecules up to 50×10^{-6} M, with the lowest detection limit of 100×10^{-9} M (Figure 14c). The increase in the conductance through p-channel is believed to

be due to the charge interaction between the biomolecule and free electron in the terminal groups of MXene. Furthermore, primary hippocampal neurons were successfully cultured for one week on the ultrathin MXene micropatterns, which shows a great bio-compatibility and their potential in bio-sensing applications. The surface of MXene micropatterns was treated by poly-L-lysine and laminin prior to long-term culture for better adhesion of the neuron cells. The real-time neuronal spiking activity has been monitored that included unique peaks compared to concurrently conducted calcium imaging.

Flexible and stretchable sensors for strain or pressure are essential for next-generation electronics with wearable, flexible, and deformable features.^[119–122] MXene has also been utilized for strain sensing applications owing to their conductive characteristics and flexibility endowed by their 2D structure. Shi et al. have demonstrated highly stretchable strain sensors inspired by the “Brick-and-Mortar” structure of natural nacre using the screen printing method^[117] (Figure 14d). 2D $\text{Ti}_3\text{C}_2\text{Tx}$ MXene nanosheets and relatively longer 1D silver nanowires (AgNWs) were used as inorganic “Bricks” that ensured the conductive percolation network. Poly(dopamine) (PDA) and Ni^{2+} cations were selected as organic “Mortar” to create multiple interactions with the MXene matrix via hydrogen bonding and coordination bonding (Figure 14e). $\text{Ti}_3\text{C}_2\text{Tx}$ MXene dispersion was sequentially mixed with dopamine, NiCl_2 , and AgNWs solutions with enough reaction time. The mixture dispersion was filtrated after sonication and agitation, and the filtered material

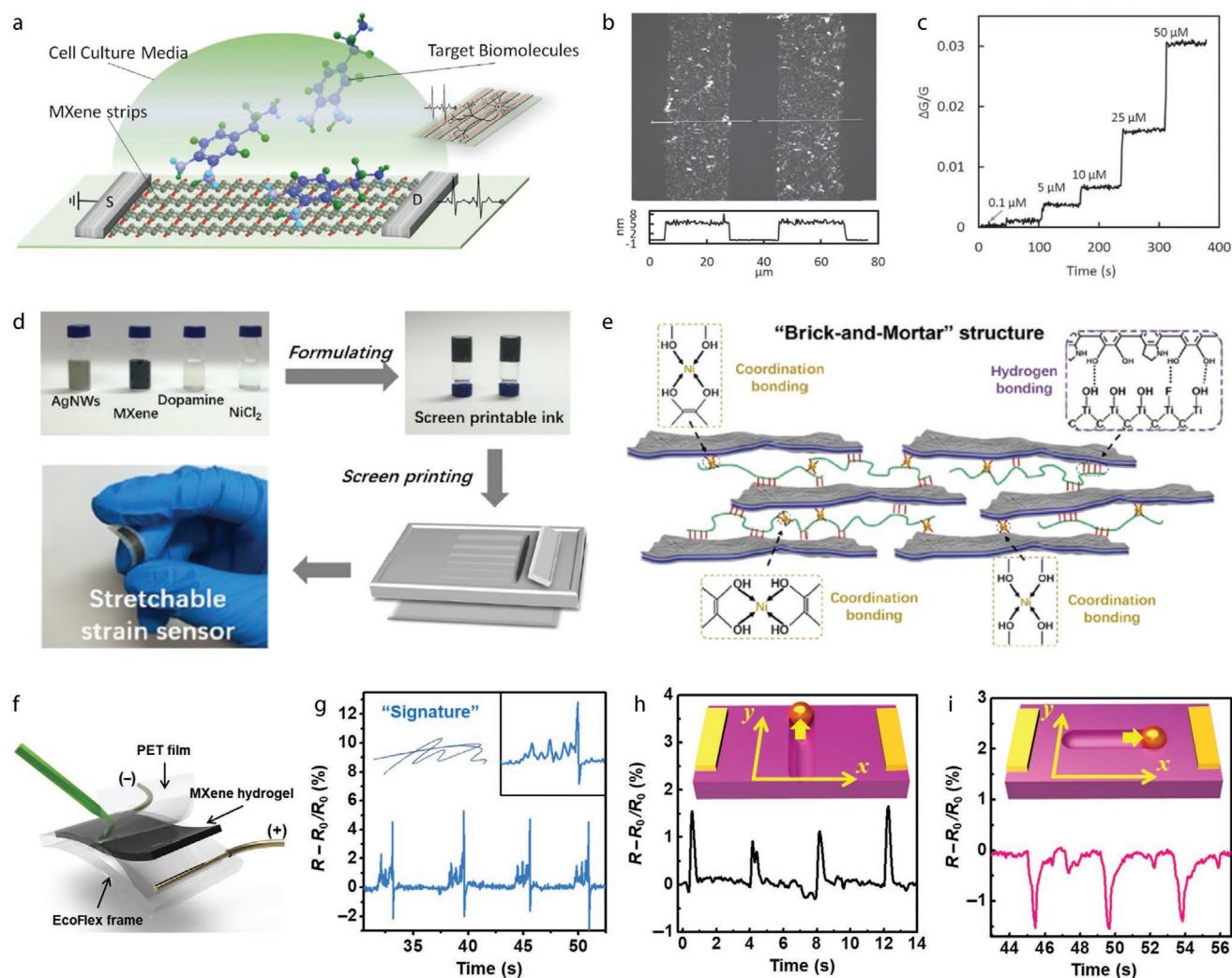


Figure 14. a) Illustration of the transfer printing process for the fabrication of MXene patterns on glass, and b) corresponding AFM image of the MXene patterns. c) The real-time monitoring of conductivity fluctuation of the printed MXene sensor for dopamine concentrations varying from 100×10^{-9} to 50×10^{-6} M. a–c) Reproduced with permission.^[116] Copyright 2016, Wiley-VCH. d) Schematic of the screen-printing fabrication process for the bioinspired $\text{Ti}_3\text{C}_2\text{T}_x$ -AgNW-PDA/ Ni^{2+} sensor and e) schematic illustration of the “brick-and-mortar” architecture. d,e) Reproduced with permission.^[117] Copyright 2019, American Chemical Society. f) Schematic for signature sensing and g) the resistance change to a signature of the MXene-hydrogel. h,i) The resistance change of M-hydrogel in response to the motion on its surface vertical to the current direction (h) and parallel to the current direction (i). Reproduced with permission.^[118] Copyright 2018, American Association for the Advancement of Science.

was washed and re-dispersed to form the screen-printable ink. The optimum mass ratio is 100:500:7:0.3 for $\text{Ti}_3\text{C}_2\text{T}_x$ /AgNWs/PDA/ Ni^{2+} . The screen-printed composite film showed a 3-fold enhancement in tensile strength and a 1.5-fold increase in fracture elongation over $\text{Ti}_3\text{C}_2\text{T}_x$ /AgNWs counterpart without PDA/ Ni^{2+} mortar; this is because MXene and PDA are weakly coupled by hydrogen bonding, which is subject of breakage at the low strain level. The incremental increase in strain resulted in further stretching of coiled polymer chains and slippage of $\text{Ti}_3\text{C}_2\text{T}_x$ /AgNWs mortar, allowing uniform accommodation of applied strain and minimization of crack propagation. The coordination bonding of Ni^{2+} /PDA- $\text{Ti}_3\text{C}_2\text{T}_x$ chelate is relatively strong; hence the strain sensor can show different sensing behavior at each strain level region. The nacre-mimic MXene strain sensor was demonstrated for the effective monitoring

of body activities and wrist pulse simultaneously. Percussion, tidal, and diastolic waves of the single heartbeat were clearly isolated and detected through electrical signals. The MXene-based strain sensor also showed highly stable results during 5000 cycles of stretching and releasing test. A small hysteresis behavior was observed that is dependent on the strain rate and was attributed to the viscoelastic behavior of PDA chains.

$\text{Ti}_3\text{C}_2\text{T}_x$ MXene has been incorporated into PVA-based hydrogel as a conductive filler for stretchable strain sensors.^[118] The addition of MXene into hydrogel resulted in one order of magnitude enhancement in the gauge factor, and both increased stretchability ($\approx 3400\%$) and self-healing ability. The MXene-PVA hydrogel shows repeatable detection of signature motion applied on its film type strain sensor (Figure 14f,g) as well as minimal strain applied on human skin such as human pulse

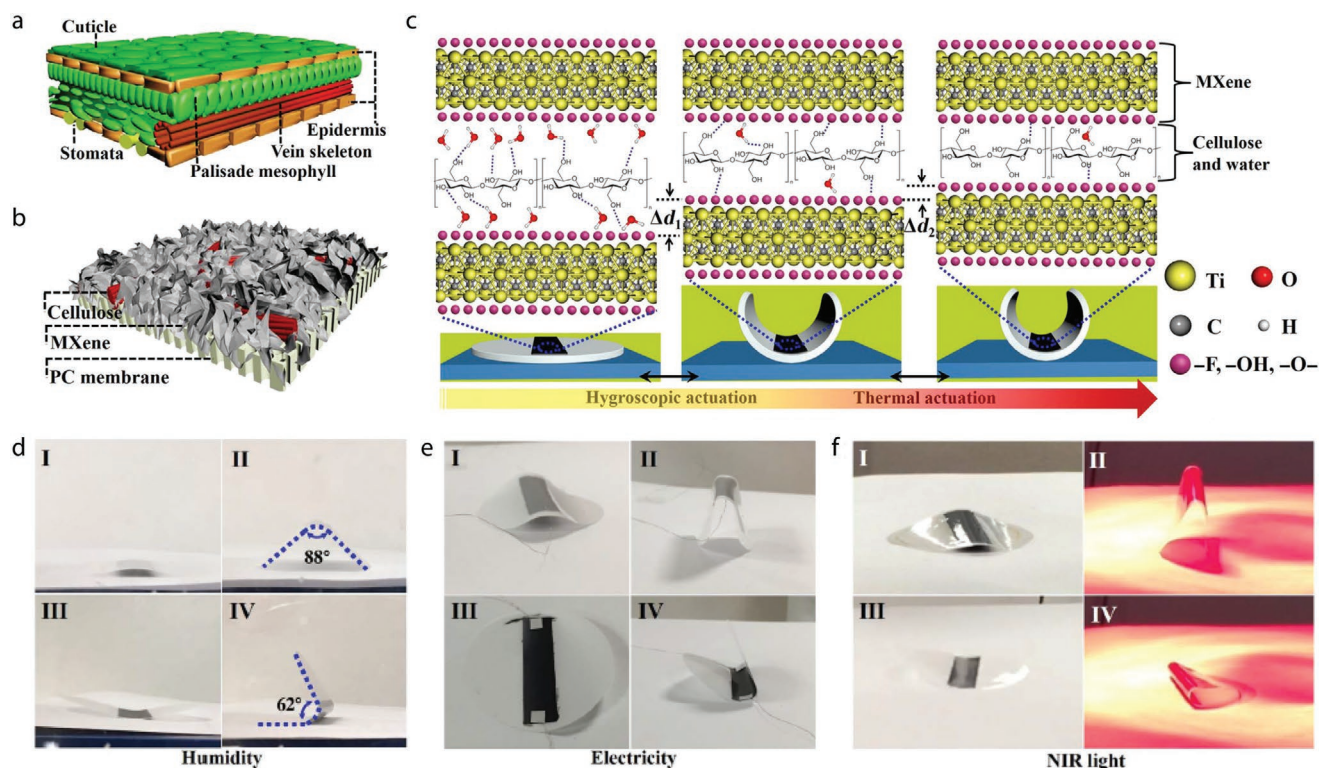


Figure 15. a) Schematic diagram of a leaf structure. b) Schematic diagram of the MXCC/PC bilayer-structured actuator, which is composed of MXCC and a PC filter membrane. c) The actuation mechanism of the MXCC/PC bilayer-structured actuator. Macroscopic and microcosmic (involving H bonds) structure changes of the MXCC/PC bilayer-structured actuator in response to hygroscopic and thermal stimuli simultaneously (both hygroscopic and thermal actuation processes are controlled by electrical and NIR light actuation). The multi-responsive performance of the MXene-based soft actuators: d) humidity-responsive capability with 70% RH for fl and flI, 10% RH for flI and flIV; the downward and upward directions refer to the actuator facing down (fl and flI) and up (flIII and flIV), respectively; e) electricity-responsive capability with power off for gl and gIII, and power on for gII and gIV; f) NIR light-responsive capability when NIR light was turned on and off with the actuator facing down (hl and hII) and up (hIII and hIV). a–f) Reproduced with permission.^[127] Copyright 2019, American Association for the Advancement of Science.

and voice of similarly sounding syllables with distinct resistance patterns. These are based on the first-time-found asymmetric strain sensitivity of MXene–PVA hydrogel (Figure 14h,i), which holds great promise for increasing the performances of hydrogel-based strain sensors. The surface functional groups of MXene, especially hydroxyl groups, were believed to play an essential role in enhancing mechanical properties.^[123,124] Once the hydrogel is under strain, the relatively weak coupling between MXenes and the polymer chains via hydrogen bonding can be partially broken, and the MXene nanosheets can dynamically rearrange in the hydrogel, in accompany with changes in electrical resistance. Such viscoelastic hydrogels also hold the potential to be mounted onto various complex surfaces and to be shaped into 3D structures via extrusion-type 3D printing.

Inkjet-printed humidity sensor of $\text{Ti}_3\text{C}_2\text{T}_x$ MXene/Ag hybrid has been reported for touchless finger motion sensing.^[125] PEDOT:PSS suspension mixed with ethylene glycol was first printed on a flexible PEN substrate as the interdigitated electrode. Poly(diallyldimethylammonium chloride) (PDDA) was then printed as the adhesive layer at the channel area between PEDOT:PSS electrodes. A mixture of $\text{Ti}_3\text{C}_2\text{T}_x$ MXene and Ag nanoparticles suspension was later printed on the PDDA layer after adjusting the viscosity. The fully inkjet-printed devices retained the transparency of $\sim 80\%$, and fast response

time with high humidity sensitivity, which enabled the detection of finger motions without contact. In a similar approach, inkjet-printed $\text{Ti}_3\text{C}_2\text{T}_x$ MXene/graphene oxide composite electrode has been reported for hydrogen peroxide (H_2O_2) sensing application with a low detection limit of $\approx 1.95 \times 10^{-6} \text{ M}$.^[126]

Owing to the hygroscopic nature of cation-intercalated $\text{Ti}_3\text{C}_2\text{T}_x$ MXene films, the multi-responsive soft actuator has been developed by mimicking the structure of natural leaves^[127] (Figure 15a,b). A mixed dispersion of MXene and cellulose fibrils was filtrated through a polycarbonate filter membrane, resulting in a bilayer structure. By using a mask during the filtration process, it was possible to pattern the film into different shapes/sizes that can control the degree of actuation. The cellulose fibrils acted as a skeleton in leaves, which helps maintain the structure and enables rapid actuation. The hydrophobic polycarbonate filter allowed the exchange of air/water molecules between the environment and MXene/cellulose film. The actuation is attributed to the interfacial stress originated from the volume changes of MXene/cellulose film as the humidity changes (Figure 15c), and the larger bending angle was due to the synergic effect of hygroscopic/thermal volume changes. The change of ambient humidity can result in a fast actuation of the bilayer system from flat (RH 70%) to bent state with a bending angle of 62–88° (RH 10%) (Figure 15d). Similar actuation can

also be triggered by running electricity through the MXene/cellulose film (Figure 15e), showing a linear dependence of bending angle to the applied electrical power. The MXene-based bilayer actuator can be operational to extreme motions at a low voltage of 5.1 V, while carbon-based ones often require more than 10 V. Moreover, NIR light irradiation can activate similar actuation in a few seconds (Figure 15f), which is based on the superior light absorption and the photothermal conversion ability of MXene. The NIR irradiation on MXene/cellulose-based actuator results in a weight decrease of only 1.7 wt%, which is much lower than the cases of polymer-based actuators (≈ 10 wt%) and is suggesting low-power consumption and rapid operation. Furthermore, Programmable-motion-actuators can be realized by the printing of MXene/cellulose ink into carefully designed shapes.

5. Conclusion and Outlook

We have reviewed recent advances in the facile patterning of MXenes for application in energy storage, electronics, optoelectronics, sensing, and actuation. Relevant printing/coating techniques and special issues related to their processes were also discussed. It is clear that publications on printing and patterned coating of MXenes are at the cusp of exponential growth. This trend is driven by: 1) the vast knowledge that has been accumulated in the past few years regarding solution processing of MXenes and the know-how to improve their stability and rheological/morphological properties; 2) the strong need for large scale, reproducible and cost-effective patterning methods of MXenes to increase device performance and to facilitate commercialization potential.

As shown by both experimental and theoretical studies, MXenes possess attractive electrochemical, electronic, optical, thermoelectric, and mechanical properties, which vary a lot by MXene composition and surface chemistry. However, so far, only one type of MXenes ($\text{Ti}_3\text{C}_2\text{T}_x$)—out of the potential dozens—has been printed. Furthermore, the present works mostly focus on printing MXene as electrodes for supercapacitors, leaving a lot of applications open to further inquiry. Given the large variety of transition metals and surface terminations, endless possibilities are anticipated to result from the tuning of composition and chemistry, and consequently, properties and applications of MXenes. One exciting direction is printing heterostructures comprising MXenes and other 2D nanomaterials, which has not yet been explored.

Given the MXenes field is still in its infancy, a lot of fundamental issues are still not fully understood. For example, it is challenging to synthesize MXenes with controllable and uniform surface terminations; however, these terminations are crucial for optimizing the rheological properties and stability of MXene inks, as well as for the performance of the obtained printed devices. To achieve this goal, all the stages in the printing process chain, including etching, delamination, size-sorting, postsynthesis treatments (e.g., chemical modifications and heating) need to be carefully tuned. So far, very few studies have been conducted regarding the correlation between the morphological/rheological properties and printed/coated device performance. This, however, is important for developing printed/coated

MXenes devices, which is a fast-emerging field that requires efforts on both experimental and theoretical domains.

On a practical level, although the colloidal stability and anti-oxidation ability of MXenes has significantly been improved in the past years, the stability of MXene inks is still far from being industrially relevant, with a shelf life of only a few months under carefully protected storage conditions. Scalability is another issue facing MXene inks, although several alternatives have been demonstrated, the highly toxic hydrofluoric acid is still the mainstream etching agent to produce MXenes, making the industrialization of MXene inks highly difficult. So far, the batch size of MXenes is still on the gram level, so there is a long way to go before it reaches industrially relevant quantities.

At this early stage of development, only a few printing and coating methods have been used to deposit/pattern MXenes. Although some reported devices have shown outstanding performance, most efforts have been confined to laboratory-scale research activity, which must be scaled up for real-world applications. For instance, no report exists on printing MXene using roll-to-roll methods, which is crucial for industrialization; the high power of printing, especially 3D printing for the construction of novel materials assembly/device structure/multifunctionality remains to be explored; due to the different feature size and requirement on inks, the combination of different printing and patterned coating technologies could offer faster production speed and more complex printed structure that enable the integration of different devices (e.g., energy storage and electronic devices). Efforts on this front are necessary. Ultimately, detailed studies on the optimization of inks and printing/coating processes are urgently needed. Looking into the future, the particular finely detailed patterning capability of printing will lead to improved device performance, lower manufacturing cost, easy integration, and miniaturization of a variety of devices based on MXenes.

Acknowledgements

Y.-Z.Z., Y.W., and Q.J. contributed equally to this work. The research reported in this publication was supported by King Abdullah University of Science & Technology (KAUST).

Conflict of Interest

The authors declare no conflict of interest.

Keywords

MXene coating, MXene patterning, MXene printing, MXenes, printing electronics

Received: December 27, 2019

Revised: February 18, 2020

Published online:

[1] H. Zhang, *ACS Nano* **2015**, 9, 9451.

[2] C. Tan, X. Cao, X.-J. Wu, Q. He, J. Yang, X. Zhang, J. Chen, W. Zhao, S. Han, G.-H. Nam, *Chem. Rev.* **2017**, 117, 6225.

- [3] K. Novoselov, A. Mishchenko, A. Carvalho, A. C. Neto, *Science* **2016**, 353, aac9439.
- [4] F. Bonaccorso, A. Bartolotta, J. N. Coleman, C. Backes, *Adv. Mater.* **2016**, 28, 6136.
- [5] G. Hu, J. Kang, L. W. Ng, X. Zhu, R. C. Howe, C. G. Jones, M. C. Hersam, T. Hasan, *Chem. Soc. Rev.* **2018**, 47, 3265.
- [6] X. Cai, Y. Luo, B. Liu, H.-M. Cheng, *Chem. Soc. Rev.* **2018**, 47, 6224.
- [7] D. Li, W. Y. Lai, Y. Z. Zhang, W. Huang, *Adv. Mater.* **2018**, 30, 1704738.
- [8] A. Kamysny, S. Magdassi, *Chem. Soc. Rev.* **2019**, 48, 1712.
- [9] A. Velasco-Hogan, J. Xu, M. A. Meyers, *Adv. Mater.* **2018**, 30, 1800940.
- [10] Y. S. Rim, S. H. Bae, H. Chen, N. De Marco, Y. Yang, *Adv. Mater.* **2016**, 28, 4415.
- [11] Y. Wang, Y.-Z. Zhang, Y.-Q. Gao, G. Sheng, J. E. ten Elshof, *Nano Energy* **2020**, 68, 104306.
- [12] T. Cheng, Y.-Z. Zhang, J.-P. Yi, L. Yang, J.-D. Zhang, W.-Y. Lai, W. Huang, *J. Mater. Chem. A* **2016**, 4, 13754.
- [13] D. Song, A. Mahajan, E. B. Secor, M. C. Hersam, L. F. Francis, C. D. Frisbie, *ACS Nano* **2017**, 11, 7431.
- [14] M. G. Mohammed, R. Kramer, *Adv. Mater.* **2017**, 29, 1604965.
- [15] M. Berggren, D. Nilsson, N. D. Robinson, *Nat. Mater.* **2007**, 6, 3.
- [16] F. Torrisi, T. Hasan, W. Wu, Z. Sun, A. Lombardo, T. S. Kulmala, G.-W. Hsieh, S. Jung, F. Bonaccorso, P. J. Paul, *ACS Nano* **2012**, 6, 2992.
- [17] Y.-Z. Zhang, Y. Wang, T. Cheng, L.-Q. Yao, X. Li, W.-Y. Lai, W. Huang, *Chem. Soc. Rev.* **2019**, 48, 3229.
- [18] K.-H. Choi, D. B. Ahn, S.-Y. Lee, *ACS Energy Lett.* **2018**, 3, 220.
- [19] F. Brunetti, A. Operamolla, S. Castro-Hermosa, G. Lucarelli, V. Manca, G. M. Farinola, T. M. Brown, *Adv. Funct. Mater.* **2019**, 29, 1806798.
- [20] S. K. Garlapati, M. Divya, B. Breitung, R. Kruk, H. Hahn, S. Dasgupta, *Adv. Mater.* **2018**, 30, 1707600.
- [21] J. Zhao, Y. Z. Zhang, F. Zhang, H. Liang, F. Ming, H. N. Alshareef, Z. Gao, *Adv. Energy Mater.* **2019**, 9, 1803215.
- [22] M. Naguib, V. N. Mochalin, M. W. Barsoum, Y. Gogotsi, *Adv. Mater.* **2014**, 26, 992.
- [23] J. Pang, R. G. Mendes, A. Bachmatiuk, L. Zhao, H. Q. Ta, T. Gemming, H. Liu, Z. Liu, M. H. Rummeli, *Chem. Soc. Rev.* **2019**, 48, 72.
- [24] K. Hantanasirisakul, Y. Gogotsi, *Adv. Mater.* **2018**, 30, 1804779.
- [25] B. Anasori, M. R. Lukatskaya, Y. Gogotsi, *Nat. Rev. Mater.* **2017**, 2, 16098.
- [26] M. Naguib, M. Kurtoglu, V. Presser, J. Lu, J. Niu, M. Heon, L. Hultman, Y. Gogotsi, M. W. Barsoum, *Adv. Mater.* **2011**, 23, 4248.
- [27] M. Alhabeb, K. Maleski, B. Anasori, P. Lelyukh, L. Clark, S. Sin, Y. Gogotsi, *Chem. Mater.* **2017**, 29, 7633.
- [28] J. Orangi, F. Hamade, V. A. Davis, M. Beidaghi, *ACS Nano* **2020**, 14, 640.
- [29] M. Naguib, O. Mashtalir, J. Carle, V. Presser, J. Lu, L. Hultman, Y. Gogotsi, M. W. Barsoum, *ACS Nano* **2012**, 6, 1322.
- [30] M. Ghidui, M. Naguib, C. Shi, O. Mashtalir, L. Pan, B. Zhang, J. Yang, Y. Gogotsi, S. J. Billinge, M. W. Barsoum, *Chem. Commun.* **2014**, 50, 9517.
- [31] O. Mashtalir, M. Naguib, V. N. Mochalin, Y. Dall'Agnese, M. Heon, M. W. Barsoum, Y. Gogotsi, *Nat. Commun.* **2013**, 4, 1716.
- [32] J. Halim, S. Kota, M. R. Lukatskaya, M. Naguib, M.-Q. Zhao, E. J. Moon, J. Pitock, J. Nanda, S. J. May, Y. Gogotsi, M. W. Barsoum, *Adv. Funct. Mater.* **2016**, 26, 3118.
- [33] B. Anasori, Y. Xie, M. Beidaghi, J. Lu, B. C. Hosler, L. Hultman, P. R. Kent, Y. Gogotsi, M. W. Barsoum, *ACS Nano* **2015**, 9, 9507.
- [34] J. Halim, M. R. Lukatskaya, K. M. Cook, J. Lu, C. R. Smith, L.-Å. Näslund, S. J. May, L. Hultman, Y. Gogotsi, P. Eklund, *Chem. Mater.* **2014**, 26, 2374.
- [35] M. Ghidui, M. R. Lukatskaya, M.-Q. Zhao, Y. Gogotsi, M. W. Barsoum, *Nature* **2014**, 516, 78.
- [36] A. Lipatov, M. Alhabeb, M. R. Lukatskaya, A. Boson, Y. Gogotsi, A. Sinitskii, *Adv. Electron. Mater.* **2016**, 2, 1600255.
- [37] M. W. Barsoum, T. El-Raghy, L. Farber, M. Amer, R. Christini, A. Adams, *J. Electrochem. Soc.* **1999**, 146, 3919.
- [38] T. Li, L. Yao, Q. Liu, J. Gu, R. Luo, J. Li, X. Yan, W. Wang, P. Liu, B. Chen, *Angew. Chem., Int. Ed.* **2018**, 57, 6115.
- [39] M. Ashton, K. Mathew, R. G. Hennig, S. B. Sinnott, *J. Phys. Chem. C* **2016**, 120, 3550.
- [40] M. Khazaei, M. Arai, T. Sasaki, C. Y. Chung, N. S. Venkataramanan, M. Estili, Y. Sakka, Y. Kawazoe, *Adv. Funct. Mater.* **2013**, 23, 2185.
- [41] J. L. Hart, K. Hantanasirisakul, A. C. Lang, B. Anasori, D. Pinto, Y. Pivak, J. T. van Ommen, S. J. May, Y. Gogotsi, M. L. Taheri, *Nat. Commun.* **2019**, 10, 522.
- [42] E. Kayali, A. VahidMohammadi, J. Orangi, M. Beidaghi, *ACS Appl. Mater. Interfaces* **2018**, 10, 25949.
- [43] J. Kang, V. K. Sangwan, J. D. Wood, M. C. Hersam, *Acc. Chem. Res.* **2017**, 50, 943.
- [44] K. Maleski, C. E. Ren, M.-Q. Zhao, B. Anasori, Y. Gogotsi, *ACS Appl. Mater. Interfaces* **2018**, 10, 24491.
- [45] K. Maleski, V. N. Mochalin, Y. Gogotsi, *Chem. Mater.* **2017**, 29, 1632.
- [46] X. Li, Z. Huang, C. Zhi, *Front. Mater.* **2019**, 6, 312.
- [47] C. J. Zhang, S. Pinilla, N. McEvoy, C. P. Cullen, B. Anasori, E. Long, S.-H. Park, A. S. Seral-Ascaso, A. Shmeliov, D. Krishnan, *Chem. Mater.* **2017**, 29, 4848.
- [48] O. Mashtalir, K. M. Cook, V. N. Mochalin, M. Crowe, M. W. Barsoum, Y. Gogotsi, *J. Mater. Chem. A* **2014**, 2, 14334.
- [49] T. Habib, X. Zhao, S. A. Shah, Y. Chen, W. Sun, H. An, J. L. Lutkenhaus, M. Radovic, M. J. Green, *npj 2D Mater. Appl.* **2019**, 3, 8.
- [50] X. Zhao, A. Vashisth, E. Prehn, W. Sun, S. A. Shah, T. Habib, Y. Chen, Z. Tan, J. L. Lutkenhaus, M. Radovic, *Matter* **2019**, 1, 513.
- [51] V. Natu, J. L. Hart, M. Sokol, H. Chiang, M. L. Taheri, M. W. Barsoum, *Angew. Chem., Int. Ed.* **2019**, 58, 12655.
- [52] B. Akuzum, K. Maleski, B. Anasori, P. Lelyukh, N. J. Alvarez, E. C. Kumbur, Y. Gogotsi, *ACS Nano* **2018**, 12, 2685.
- [53] Z. Fan, C. Wei, L. Yu, Z. Xia, J. Cai, Z. Tian, G. Zou, S. X. Dou, J. Sun, *ACS Nano* **2020**, 14, 867.
- [54] W. Yang, J. Yang, J. J. Byun, F. P. Moissinac, J. Xu, S. J. Haigh, M. Domingos, M. A. Bisset, R. A. Dryfe, S. Barg, *Adv. Mater.* **2019**, 31, 1902725.
- [55] H. Li, J. Liang, *Adv. Mater.* **2019**, 32, 1805864.
- [56] C. J. Zhang, L. McKeon, M. P. Kremer, S.-H. Park, O. Ronan, A. Seral-Ascaso, S. Barwich, C. Ó. Coileáin, N. McEvoy, H. C. Nerl, *Nat. Commun.* **2019**, 10, 1795.
- [57] L. Yu, Z. Fan, Y. Shao, Z. Tian, J. Sun, Z. Liu, *Adv. Energy Mater.* **2019**, 9, 1901839.
- [58] C. Zhang, M. P. Kremer, A. Seral-Ascaso, S. H. Park, N. McEvoy, B. Anasori, Y. Gogotsi, V. Nicolosi, *Adv. Funct. Mater.* **2018**, 28, 1705506.
- [59] E. Quain, T. S. Mathis, N. Kurra, K. Maleski, K. L. Van Aken, M. Alhabeb, H. N. Alshareef, Y. Gogotsi, *Adv. Mater. Technol.* **2019**, 4, 1800256.
- [60] Y.-Y. Peng, B. Akuzum, N. Kurra, M.-Q. Zhao, M. Alhabeb, B. Anasori, E. C. Kumbur, H. N. Alshareef, M.-D. Ger, Y. Gogotsi, *Energy Environ. Sci.* **2016**, 9, 2847.
- [61] A. G. Kelly, T. Hallam, C. Backes, A. Harvey, A. S. Esmaeili, I. Godwin, J. Coelho, V. Nicolosi, J. Lauth, A. Kulkarni, *Science* **2017**, 356, 69.
- [62] D. McManus, S. Vranic, F. Withers, V. Sanchez-Romaguera, M. Macucci, H. Yang, R. Sorrentino, K. Parvez, S.-K. Son, G. Iannaccone, *Nat. Nanotechnol.* **2017**, 12, 343.

- [63] L. Hu, H. Wu, Y. Cui, *Appl. Phys. Lett.* **2010**, 96, 183502.
- [64] H. Pang, Y. Zhang, W.-Y. Lai, Z. Hu, W. Huang, *Nano Energy* **2015**, 15, 303.
- [65] Y. Wang, Y.-Z. Zhang, D. Dubbink, J. E. ten Elshof, *Nano Energy* **2018**, 49, 481.
- [66] T. Carey, S. Cacovich, G. Divitini, J. Ren, A. Mansouri, J. M. Kim, C. Wang, C. Ducati, R. Sordan, F. Torrisi, *Nat. Commun.* **2017**, 8, 1202.
- [67] D. Jang, D. Kim, J. Moon, *Langmuir* **2009**, 25, 2629.
- [68] W.-K. Hsiao, I. Hutchings, S. Hoath, G. Martin, *J. Imaging Sci. Technol.* **2009**, 53, 050304.
- [69] G. Hu, T. Albrow-Owen, X. Jin, A. Ali, Y. Hu, R. C. Howe, K. Shehzad, Z. Yang, X. Zhu, R. I. Woodward, *Nat. Commun.* **2017**, 8, 278.
- [70] H. Li, X. Li, J. Liang, Y. Chen, *Adv. Energy Mater.* **2019**, 9, 1803987.
- [71] C. Linghu, S. Zhang, C. Wang, J. Song, *npj Flexible Electron.* **2018**, 2, 26.
- [72] F. C. Krebs, *Sol. Energy Mater. Sol. Cells* **2009**, 93, 1636.
- [73] A. Russo, B. Y. Ahn, J. J. Adams, E. B. Duoss, J. T. Bernhard, J. A. Lewis, *Adv. Mater.* **2011**, 23, 3426.
- [74] R. L. Truby, J. A. Lewis, *Nature* **2016**, 540, 371.
- [75] F. Zhang, M. Wei, V. V. Viswanathan, B. Swart, Y. Shao, G. Wu, C. Zhou, *Nano Energy* **2017**, 40, 418.
- [76] J. D. Cain, A. Azizi, K. Maleski, B. Anasori, E. C. Glazer, P. Y. Kim, Y. Gogotsi, B. A. Helms, T. P. Russell, A. Zettl, *ACS Nano* **2019**, 13, 12385.
- [77] F. Aziz, A. Ismail, *Mater. Sci. Semicond. Process.* **2015**, 39, 416.
- [78] L. Hu, J. W. Choi, Y. Yang, S. Jeong, F. La Mantia, L.-F. Cui, Y. Cui, *Proc. Natl. Acad. Sci. USA* **2009**, 106, 21490.
- [79] N. Kurra, B. Ahmed, Y. Gogotsi, H. N. Alshareef, *Adv. Energy Mater.* **2016**, 6, 1601372.
- [80] Q. Jiang, N. Kurra, K. Maleski, Y. Lei, H. Liang, Y. Zhang, Y. Gogotsi, H. N. Alshareef, *Adv. Energy Mater.* **2019**, 1901061.
- [81] C. Chen, X. Xie, B. Anasori, A. Sarycheva, T. Makaryan, M. Zhao, P. Urbankowski, L. Miao, J. Jiang, Y. Gogotsi, *Angew. Chem., Int. Ed.* **2018**, 57, 1846.
- [82] D. Zhao, R. Zhao, S. Dong, X. Miao, Z. Zhang, C. Wang, L. Yin, *Energy Environ. Sci.* **2019**, 12, 2422.
- [83] P. Lian, Y. Dong, Z.-S. Wu, S. Zheng, X. Wang, S. Wang, C. Sun, J. Qin, X. Shi, X. Bao, *Nano Energy* **2017**, 40, 1.
- [84] H. Tang, W. Li, L. Pan, C. P. Cullen, Y. Liu, A. Pakdel, D. Long, J. Yang, N. McEvoy, G. S. Duesberg, V. Nicolosi, C. Zhang, *Adv. Sci.* **2018**, 5, 1800502.
- [85] H. Tang, W. Li, L. Pan, K. Tu, F. Du, T. Qiu, J. Yang, C. P. Cullen, N. McEvoy, C. Zhang, *Adv. Funct. Mater.* **2019**, 29, 1901907.
- [86] G. Wang, L. Zhang, J. Zhang, *Chem. Soc. Rev.* **2012**, 41, 797.
- [87] Y. Z. Zhang, T. Cheng, Y. Wang, W. Y. Lai, H. Pang, W. Huang, *Adv. Mater.* **2016**, 28, 5242.
- [88] Y.-Z. Zhang, Y. Wang, Y.-L. Xie, T. Cheng, W.-Y. Lai, H. Pang, W. Huang, *Nanoscale* **2014**, 6, 14354.
- [89] M. Beidaghi, Y. Gogotsi, *Energy Environ. Sci.* **2014**, 7, 867.
- [90] C.-W. Wu, B. Unnikrishnan, I.-W. P. Chen, S. G. Harroun, H.-T. Chang, C.-C. Huang, *Energy Storage Mater.* **2020**, 25, 563.
- [91] S. Xu, Y. Dall'Agnese, G. Wei, C. Zhang, Y. Gogotsi, W. Han, *Nano Energy* **2018**, 50, 479.
- [92] Y.-Z. Zhang, Y. Wang, T. Cheng, W.-Y. Lai, H. Pang, W. Huang, *Chem. Soc. Rev.* **2015**, 44, 5181.
- [93] N. Wang, J. Liu, Y. Zhao, M. Hu, R. Qin, G. Shan, *ChemNanoMat* **2019**, 5, 658.
- [94] S. Jiao, A. Zhou, M. Wu, H. Hu, *Adv. Sci.* **2019**, 6, 1900529.
- [95] H. Huang, X. Chu, H. Su, H. Zhang, Y. Xie, W. Deng, N. Chen, F. Liu, H. Zhang, B. Gu, W. Deng, W. Yang, *J. Power Sources* **2019**, 415, 1.
- [96] C. J. Zhang, S.-H. Park, A. Seral-Ascaso, S. Barwich, N. McEvoy, C. S. Boland, J. N. Coleman, Y. Gogotsi, V. Nicolosi, *Nat. Commun.* **2019**, 10, 849.
- [97] G. Li, K. Kushnir, Y. Dong, S. Chertopalov, A. M. Rao, V. N. Mochalin, R. Podila, L. V. Titova, *2D Mater.* **2018**, 5, 035043.
- [98] K. Shen, B. Li, S. Yang, *Energy Storage Mater.* **2020**, 24, 670.
- [99] Z. Wang, H. Kim, H. N. Alshareef, *Adv. Mater.* **2018**, 30, 1706656.
- [100] H. Kim, Z. Wang, H. N. Alshareef, *Nano Energy* **2019**, 60, 179.
- [101] W. Sun, Y. Xie, P. R. Kent, *Nanoscale* **2018**, 10, 11962.
- [102] A. Sarycheva, A. Polemi, Y. Liu, K. Dandekar, B. Anasori, Y. Gogotsi, *Sci. Adv.* **2018**, 4, eaau0920.
- [103] S. Lopatin, J. K. El-Demellawi, H. N. Alshareef, *Microsc. Microanal.* **2018**, 24, 1578.
- [104] D. B. Velusamy, J. K. El-Demellawi, A. M. El-Zohry, A. Giugni, S. Lopatin, M. N. Hedhili, A. E. Mansour, E. D. Fabrizio, O. F. Mohammed, H. N. Alshareef, *Adv. Mater.* **2019**, 31, 1807658.
- [105] J. K. El-Demellawi, S. Lopatin, J. Yin, O. F. Mohammed, H. N. Alshareef, *ACS Nano* **2018**, 12, 8485.
- [106] K. Chaudhuri, M. Alhabeb, Z. Wang, V. M. Shalae, Y. Gogotsi, A. Boltasseva, *ACS Photonics* **2018**, 5, 1115.
- [107] M. Vural, A. Pena-Francesch, J. Bars-Pomes, H. Jung, H. Gudapati, C. B. Hatter, B. D. Allen, B. Anasori, I. T. Ozbolat, Y. Gogotsi, *Adv. Funct. Mater.* **2018**, 28, 1801922.
- [108] X. Jiang, W. Li, T. Hai, R. Yue, Z. Chen, C. Lao, Y. Ge, G. Xie, Q. Wen, H. Zhang, *npj 2D Mater. Appl.* **2019**, 3, 1.
- [109] A. Sinha, H. Zhao, Y. Huang, X. Lu, J. Chen, R. Jain, *TrAC, Trends Anal. Chem.* **2018**, 105, 424.
- [110] Y. Cai, J. Shen, G. Ge, Y. Zhang, W. Jin, W. Huang, J. Shao, J. Yang, X. Dong, *ACS Nano* **2018**, 12, 56.
- [111] S. J. Kim, H.-J. Koh, C. E. Ren, O. Kwon, K. Maleski, S.-Y. Cho, B. Anasori, C.-K. Kim, Y.-K. Choi, J. Kim, *ACS Nano* **2018**, 12, 986.
- [112] Y. Lei, W. Zhao, Y. Zhang, Q. Jiang, J. H. He, A. J. Baeumner, O. S. Wolfbeis, Z. L. Wang, K. N. Salama, H. N. Alshareef, *Small* **2019**, 15, 1901190.
- [113] R. Li, L. Zhang, L. Shi, P. Wang, *ACS Nano* **2017**, 11, 3752.
- [114] S. Umrao, R. Tabassian, J. Kim, Q. Zhou, S. Nam, I.-K. Oh, *Sci. Rob.* **2019**, 4, eaaw7797.
- [115] J. Come, J. M. Black, M. R. Lukatskaya, M. Naguib, M. Beidaghi, A. J. Rondinone, S. V. Kalinin, D. J. Wesolowski, Y. Gogotsi, N. Balke, *Nano Energy* **2015**, 17, 27.
- [116] B. Xu, M. Zhu, W. Zhang, X. Zhen, Z. Pei, Q. Xue, C. Zhi, P. Shi, *Adv. Mater.* **2016**, 28, 3333.
- [117] X. Shi, H. Wang, X. Xie, Q. Xue, J. Zhang, S. Kang, C. Wang, J. Liang, Y. Chen, *ACS Nano* **2019**, 13, 649.
- [118] Y.-Z. Zhang, K. H. Lee, D. H. Anjum, R. Sougrat, Q. Jiang, H. Kim, H. N. Alshareef, *Sci. Adv.* **2018**, 4, eaat0098.
- [119] G. Ge, Y. Zhang, J. Shao, W. Wang, W. Si, W. Huang, X. Dong, *Adv. Funct. Mater.* **2018**, 28, 1802576.
- [120] D. J. Lipomi, M. Vosgueritchian, B. C. Tee, S. L. Hellstrom, J. A. Lee, C. H. Fox, Z. Bao, *Nat. Nanotechnol.* **2011**, 6, 788.
- [121] J. T. Muth, D. M. Vogt, R. L. Truby, Y. Mengüç, D. B. Kolesky, R. J. Wood, J. A. Lewis, *Adv. Mater.* **2014**, 26, 6307.
- [122] G. Ge, Y. Cai, Q. Dong, Y. Zhang, J. Shao, W. Huang, X. Dong, *Nanoscale* **2018**, 10, 10033.
- [123] L. Z. Zhao, C. H. Zhou, J. Wang, D. S. Tong, W. H. Yu, H. Wang, *Soft Matter* **2015**, 11, 9229.
- [124] K. Haraguchi, R. Farnworth, A. Ohbayashi, T. Takehisa, *Macromolecules* **2003**, 36, 5732.
- [125] N. Li, Y. Jiang, Y. Xiao, B. Meng, C. Xing, H. Zhang, Z. Peng, *Nanoscale* **2019**, 11, 21522.
- [126] J. Zheng, J. Diao, Y. Jin, A. Ding, B. Wang, L. Wu, B. Weng, J. Chen, *J. Electrochem. Soc.* **2018**, 165, B227.
- [127] G. Cai, J.-H. Ciou, Y. Liu, Y. Jiang, P. S. Lee, *Sci. Adv.* **2019**, 5, eaaw7956.